

**Department of Physics and Astronomy  
Heidelberg University**

Master Thesis in Physics  
submitted by

**Maulik Deepen Parekh**  
born in Bhiwandi, India

submitted in  
**January, 2025**

---

# The Gas Fraction of Mock-Observed Galaxy Groups with Cosmological Simulations

---

This Master Thesis has been carried out by Maulik Deepen Parekh at the  
**Max-Planck-Institute for Astronomy** in Heidelberg  
under the supervision of  
**Dr. Urmila Chadayammuri & Dr. Annalisa Pillepich**

## **Abstract**

In the context of understanding the distribution of baryonic matter in the universe and its implications on understanding cosmology, galaxy groups are of significant importance. Observational surveys in X-rays are primed to analyse the gas distribution and properties in galaxy groups. However, due to instrumental limits in detecting flux, observations can have selection biases that affect the inferences made from their analysis. Modern cosmological simulations have successfully modeled the underlying physics behind the formation and evolution of galactic structures. In this work, we perform mock observations of simulated galaxy groups in three simulations: IllustrisTNG suite's 100 Mpc box (TNG100), SIMBA, and EAGLE. Through these, we study the effects of the observations on the intrinsic gas fraction ( $f_g$ ) of the galaxy groups at  $z = 0$  in the simulations. We find that within the statistical range of  $1 - \sigma$  standard deviation, the mock-observed groups follow the same relation of  $f_g - M_{200c}$  as the underlying population of groups in all simulations. Hence, the limits in detection, when modeled correctly, do not affect the inferences of the  $f_g - M_{200c}$  relation.

## **Zusammenfassung**

Für das Verständnis der Verteilung baryonischer Materie im Universum und ihrer Implikationen für das Verständnis der Kosmologie sind Galaxienhaufen von erheblicher Bedeutung. Beobachtungsstudien im Röntgenbereich sind darauf ausgerichtet, die Gasverteilung und Eigenschaften von Galaxienhaufen zu analysieren. Aufgrund instrumenteller Beschränkungen bei der Lichtstromdetektion können Beobachtungen jedoch Selektionsverzerrungen aufweisen, die die aus ihrer Analyse gezogenen Schlussfolgerungen beeinflussen. Moderne kosmologische Simulationen haben die zugrundeliegende Physik der Entstehung und Entwicklung galaktischer Strukturen erfolgreich modelliert. In dieser Arbeit werden Scheinbeobachtungen von simulierten Galaxienhaufen in drei Simulationen durchgeführt: IllustrisTNG-Suite's 100 Mpc Box (TNG100), SIMBA und EAGLE. Mit diesen werden die Auswirkungen der Beobachtungen auf die intrinsische Gasanteil ( $f_g$ ) der Galaxienhaufen bei  $z = 0$  in den Simulationen untersucht. Das Ergebnis dieser Arbeit ist, dass die scheinbeobachteten Galaxienhaufen innerhalb des statistischen  $1 - \sigma$ -Bereichs der gleichen Beziehung von  $f_g - M_{200c}$  folgen wie die zugrundeliegende Population von Galaxienhaufen in allen Simulationen. Folglich beeinflussen die instrumentellen Beschränkungen, sofern sie korrekt modelliert werden, die Schlussfolgerungen der  $f_g - M_{200c}$ -Beziehung nicht.

# Contents

<b>1</b>	<b>Introduction and motivation</b>	<b>1</b>
1.1	Galaxy groups . . . . .	1
1.2	Observing galaxy groups across wavelengths . . . . .	4
1.3	X-ray observatories considered in this thesis . . . . .	5
1.3.1	Chandra X-ray Observatory . . . . .	5
1.3.2	XMM-Newton . . . . .	6
1.3.3	eROSTIA . . . . .	6
1.4	Simulating galaxy groups in the full cosmological context . . . . .	7
1.4.1	Cosmological model and initial conditions . . . . .	8
1.4.2	Solving gravity . . . . .	8
1.4.3	Solving hydrodynamics . . . . .	8
1.5	The simulations of galaxy groups of this thesis . . . . .	9
1.5.1	IllustrisTNG . . . . .	9
1.5.2	SIMBA . . . . .	10
1.5.3	EAGLE . . . . .	10
<b>2</b>	<b>Diverse gas properties in groups from different state-of-the-art simulations</b>	<b>11</b>
2.1	Total gas properties in halos . . . . .	11
2.2	Radial gas profiles . . . . .	14
2.3	Intrinsic X-ray luminosity . . . . .	17
2.4	Differences in the physical models of the simulations that affect the gas distribution in groups . . . . .	21
<b>3</b>	<b>From simulated data to X-ray observations of galaxy groups</b>	<b>25</b>
3.1	Simulated data to intrinsic observable . . . . .	25
3.2	Creating ideal mocks . . . . .	27
3.3	Creating Chandra mocks . . . . .	28
3.4	Creating XMM-Newton and eROSITA mocks . . . . .	28
3.4.1	Notes . . . . .	29
3.5	Calculating X-ray luminosity . . . . .	30

*Contents*

<b>4 Observational effects on the inference of the gas content of X-ray detected galaxy groups</b>	<b>33</b>
4.1 Chandra mocks . . . . .	34
4.2 XMM-Newton mocks . . . . .	35
4.3 eROSITA mocks . . . . .	36
4.4 Mocked X-ray luminosity . . . . .	37
4.5 Effects of detection on the inferred relationship between gas fraction and total mass . . . . .	41
4.5.1 Chandra . . . . .	41
4.5.2 XMM-Newton . . . . .	43
4.5.3 eROSITA . . . . .	44
<b>5 Summary, Conclusion, and Outlook</b>	<b>49</b>
<b>6 Acknowledgements</b>	<b>51</b>

# 1 Introduction and motivation

## 1.1 Galaxy groups

The study of the large-scale structure of the universe has been of great importance in understanding cosmological as well as astrophysical phenomena that lead to cosmic structure formation. Groups and clusters of galaxies are some of the largest collapsed structures in the universe. Galaxy groups consist of a few tens of galaxies bound in a common gravitational potential. Since structure formation in the universe is hierarchical, meaning that smaller structures form first and then merge to form larger structures, galaxy groups dominate the halo mass function over clusters (Figure 1.1) and contain a significant fraction of the overall universal baryon budget. Being less massive than clusters, the energy that is supplied by supernovae and active galactic nuclei (**AGNs**) to the hot intra-group medium (**IGrM**) can easily exceed their gravitational binding energy. Thus, it is expected that these non-gravitational mechanisms have a strong effect on the distribution of the baryons ([Wri+24]; [ANP23]), making galaxy groups ideal targets to constrain these mechanisms. The net effect of the various feedback processes in action in the gravitational potential wells is to change the radial distribution of the energy and mass in groups, affecting the correlations between their observed properties ([Lov+21]). When studying the galaxy group regime, since we have many more galaxy groups than clusters, they offer enough data points to narrow down the statistical uncertainties in the inferences, hence increasing precision. Thus, the variation in different models for different phenomena is then dependent on systematic effects, making galaxy groups key to our understanding of the systematics of how matter is distributed in the universe.

### 1.1 Galaxy groups

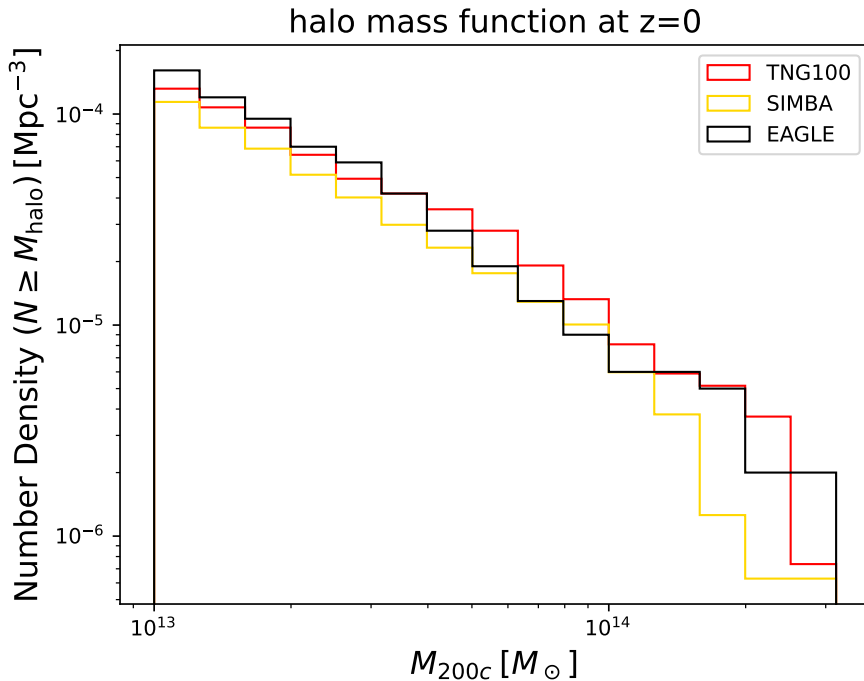


**Figure 1.1.** The halo mass function in the galaxy group and cluster regime in the simulations.

To classify galaxy groups in this thesis, we follow these steps:

- The simulations have data stored in two divisions, the snapshot data and the group catalog data.
- Furthermore, the group catalog uses a friends-of-friends (FOF) algorithm to classify '**FOF halos**', also known as '**FOF groups**', or '**halos**'.
- We select these halos, which then have multiple fields associated with them.
- The field we choose to work with is the  $M_{200c}$  field, which stores the mass contained within the sphere of radius  $r_{200c}$  of the halo.  $r_{200c}$  is calculated as the distance from the center of the halo where its mass density is 200 times the critical energy density ( $\rho_{\text{crit}}$ ) of the universe.
- The halos chosen to analyse galaxy groups are the ones with an  $M_{200c}$  **in the range of  $10^{13}$  to  $10^{14}$   $M_\odot$** .

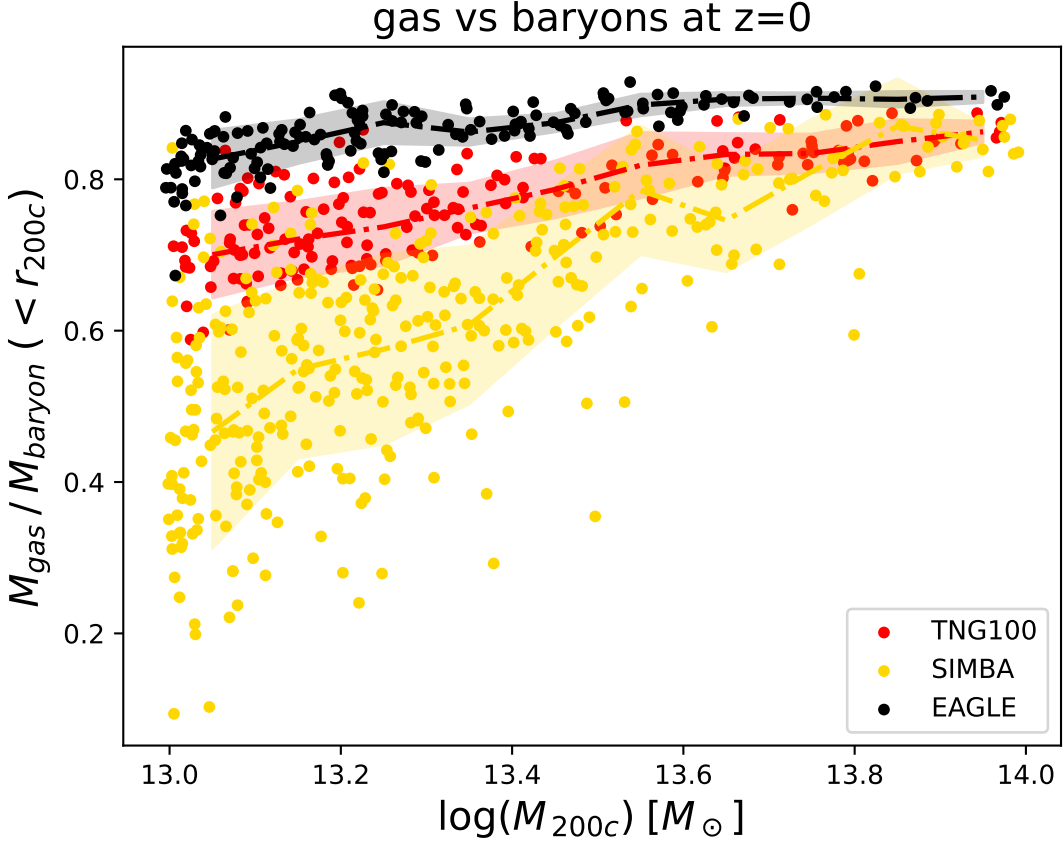


**Figure 1.2.** Ratio of the gas mass inside  $r_{200c}$  and the baryon mass (gas + stars + black holes) inside  $r_{200c}$  as a function of  $M_{200c}$  from the IllustrisTNG-100, EAGLE, and SIMBA simulations.

Gas properties in the IGrM depend on the amount of gas available in the galaxy group and this can be quantified by calculating the gas fraction ( $f_g$ ), i.e. the ratio of the total gas mass in the halo over the total mass in the halo, which is then normalized to the cosmic average baryon fraction, as most of the baryonic mass in halos at this mass range is in the gas (Figure 1.2). This is challenged at the low mass end of the galaxy groups, especially in the SIMBA simulation data, but we still use  $f_g$  from now on, in line with the literature, since we observe the X-ray regime emitted by the hot gas ( $> 10^5$  K) in the groups and clusters. The cosmic average baryon fraction ( $\Omega_b/\Omega_m$ ) used is 0.16, which is similar to the value in all the three simulations used (IllustrisTNG: [Pil+18]; SIMBA: [Dav+19]; EAGLE: [Sch+15b]).

## 1.2 Observing galaxy groups across wavelengths

Observational surveys targeting galaxy groups try to understand a plethora of processes in them. These include structure formation and the processes driving the formation of groups, the nature and distribution of mass in and around the groups, the distribution and properties of the gas in the IGrM, the evolution of groups and the effects of the environment, understanding the interplay between the gravitational collapse and the baryonic processes of stellar feedback, growth and feedback of the AGN, and the distribution of groups in the large scale structure, which can then be used to constrain cosmological parameters. These surveys use different regions of the electromagnetic spectrum to probe and study the distribution and properties of galaxy groups, and they span a range of redshifts to study the evolution of these properties. The predominant ones are X-ray and SZ surveys, often complemented by optical surveys.

X-ray observations use the soft band X-ray emission, i.e. 0.5-2 keV emission, to study the properties of hot gas around groups and the temperature distribution of the gas, which provide information about the mass and the gas fraction in the groups as a function of their radius and total mass. Observations collect the soft band photon position (RA, DEC) and energy and then convert the total energy into a flux using a conversion factor calculated based on the instrumental response. The flux can then be converted to a luminosity ( $L_x$ ) using the redshift data for the source objects with the relation  $L_x = 4\pi d_L^2$ , where  $d_L$  is the luminosity distance of the source. The  $L_x$  is then used to obtain the temperature and mass profiles. The X-ray scaling relations for galaxy systems (such as  $L_x - M$ ,  $L_x - T$ , etc.) were derived ([Kai86]; [BDC12]; [ELS20]), based on the simple assumption that the thermodynamic properties of the intra-cluster medium (**ICM**) are only determined by gravity (i.e., gas just follows the dark matter collapse). Since gravity is scale-free, this model predicts that objects of different sizes are the scaled version of each other. This is also known as the self-similar model. However, since groups are dominated by baryonic processes, the corrections in the scaling relations need to be accounted for. Observations for these scaling relations need to be further corrected for the biases introduced due to selection effects since X-ray observations are often flux-limited, which means that objects below the limiting flux value are not detected. For a given redshift, this means that objects below a limiting  $L_x$  value will not be detected.

To assess the extent of this bias, we can use mock observations from realistic cosmological simulations. With large-scale cosmological simulations, we can track all the intrinsic properties of the galaxy groups across redshifts and hence get a good picture of the different processes affecting the evolution of groups. We discuss cosmological simulations in the later sections.

## 1.3 X-ray observatories considered in this thesis

We make use of data from three X-ray observatories in this thesis, namely, Chandra, XMM-Newton, and eROSITA. Table 1.1 shows the comparison of the properties in the three observatories.

---

Observatory	Energy range	Field of view	Angular resolution	Effective area
Chandra <sup>(a)</sup>	0.1-10 keV	17'	0.5''	400 cm <sup>2</sup> @ 1 keV
XMM-Newton <sup>(b)</sup>	0.15-12 keV	30'	15''	1500 cm <sup>2</sup> @ 1keV
eROSITA <sup>(c)</sup>	0.2-10 keV	1°	30''	1365 cm <sup>2</sup> @ 1 keV

---

**Table 1.1.** The properties of the observatories used in this thesis.

(a) Chandra specifications can be found at [chandra.harvard.edu/about/specs.html](http://chandra.harvard.edu/about/specs.html)

(b) XMM-Newton details can be found at [cosmos.esa.int/web/xmm-newton/technical-details](http://cosmos.esa.int/web/xmm-newton/technical-details)

(c) eROSITA details can be found at [erosita.mpe.mpg.de/edr/index.php](http://erosita.mpe.mpg.de/edr/index.php)

### 1.3.1 Chandra X-ray Observatory

The Chandra X-ray Observatory (CXO) launched in 1999, has provided unprecedented capabilities for sub-arcsecond imaging, spectrometric imaging, and high-resolution dispersive spectroscopy ([Wei+02]). Chandra uses four pairs of nested mirrors, together with their support structure, called the High-Resolution Mirror Assembly (HRMA). Aft of the HRMA are two objective transmission gratings: the Low-Energy Transmission Grating (LETG) and the High-Energy Transmission Grating (HETG). The Science Instrument Module (SIM) holds the two focal plane instruments, the Advanced CCD Imaging Spectrometer (ACIS) ([Gar+03]) operating in the photon energy range of 0.2 – 10 keV, and the High-Resolution Camera (HRC). ACIS-I is made of a  $2 \times 2$  array of charge-coupled-devices (CCDs) and provides high-resolution spectrometric imaging over a 17 arcmin square field of view (FoV). ACIS-S is a  $6 \times 1$  array of CCDs and serves as the primary readout detector for the HETG, and also provides high-resolution spectrometric imaging extending to lower energies but over a smaller (8 arcmin) field than ACIS-I. Chandra's point spread function (PSF) has a full width at half-maximum (FWHM) less than 0.5 arcsec.

### 1.3.2 XMM-Newton

XMM-Newton was a cornerstone project in the ESA Horizon 2000 program launched in 1999 ([LJS12]; [Jan+01]). Each of the three X-ray telescopes on board XMM-Newton consists of 58 Wolter I mirrors which are nested in a coaxial and confocal configuration, with an effective area of  $1500 \text{ cm}^2$  at 1.5 keV and  $580 \text{ cm}^2$  at 8 keV. The instruments on board XMM-Newton are three European Photon Imaging Cameras (EPIC) ([Str+01]; [Tur+01]), two Reflection Grating Spectrometers (RGS), and an Optical Monitor. The three European Photon Imaging Cameras (EPIC) are the primary instruments aboard XMM-Newton. The system comprises two MOS-CCD cameras and a single pn-CCD camera, with a total FoV of 30 arcmin and an energy sensitivity range of 0.15 - 12 keV. The telescope has been used to investigate interstellar X-ray sources, perform narrow and broad-range spectroscopy, and perform the first simultaneous imaging of objects in both X-ray and optical (visible and ultraviolet) wavelengths.

### 1.3.3 eROSTIA

The extended ROentgen Survey with an Imaging Telescope Array (eROSITA) was launched in 2019 ([Pre+21]). eROSITA, with its large collecting area in the soft X-ray band ( $1365 \text{ cm}^2$  at 1 keV), moderate angular resolution averaged over the FoV (26 arcsec half energy width at 1.49 keV), and a circular FoV with a diameter of 1 degree, was designed as a sensitive wide-field X-ray telescope capable of delivering deep, sharp images over very large areas of the sky. It consists of seven identical and co-aligned X-ray mirror assemblies (MAs) housed in a common optical bench. Each of the mirrors comprises 54 paraboloid/hyperboloid mirror shells in a Wolter-I geometry. The eROSITA X-ray All-Sky survey (eRASS) consists of eight complete scans of the X-ray sky, each lasting for six months. The performance verification survey, eROSITA Final Equatorial-Depth Survey (eFEDS) ([Bru+22]; [Liu+22]), and the first Western All-Sky Survey of eROSITA (eRASS1) ([Mer+24]; [Bul+24]) provide a catalog of groups and clusters.

## 1.4 Simulating galaxy groups in the full cosmological context

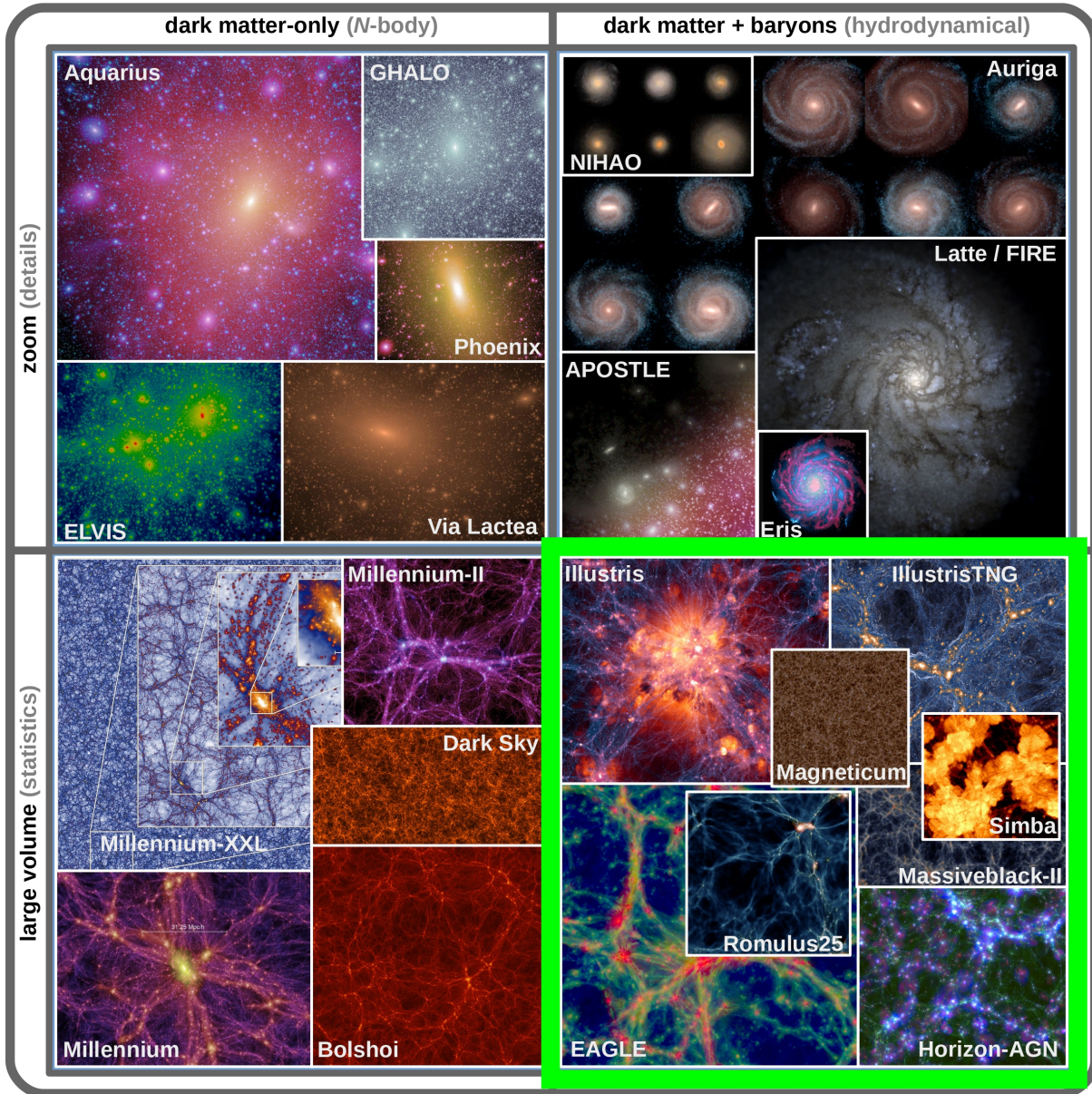


**Figure 1.3.** An overview of the different cosmological simulations. The green highlighted region shows the kind of simulations relevant to this thesis. Figure taken from [Vog+20].

Cosmological simulations of galaxy formation have been instrumental in advancing our understanding of structure and galaxy formation in the Universe. These simulations follow the non-linear evolution of galaxies, modeling a variety of physical processes over an enormous range of scales. These simulations are, hence, the method of choice for tackling the complexities when studying the properties, growth, and evolution of galaxy systems. Modern simulations model dark matter, dark energy, and ordinary matter in

an expanding space-time starting from well-defined initial conditions. The landscape of cosmological simulations is shown in Figure 1.3

### 1.4.1 Cosmological model and initial conditions

The leading model for structure formation assumes cold dark matter, and dark energy represented by a cosmological constant  $\Lambda$ , which drives the accelerated expansion of the Universe. This leads to the concordance  $\Lambda$ CDM model, which builds the framework for galaxy formation. Measurements of the cosmic microwave background combined with other observations such as the distance-redshift relation from Type Ia supernovae, abundances of galaxy clusters, and galaxy clustering constrain the fundamental parameters of the  $\Lambda$ CDM model. The simulations start from smooth initial conditions constrained through observations of the cosmic microwave background ([Pla+20]), yielding detailed predictions of the galaxy population at different epochs of the Universe.

### 1.4.2 Solving gravity

To simulate dark matter, cosmological simulations solve the collision-less Boltzmann equation coupled to Poisson's equation in an expanding background universe. Most of them employ Newtonian gravity, which provides a good approximation. They are also typically performed with periodic boundary conditions to mimic the large-scale homogeneity and isotropy of the matter distribution of the Universe. The particle dynamics are followed by an N-body method, with either the tree approach ([BH86]), the particle-mesh approach ([HE81]), or a hybrid scheme combining the two.

### 1.4.3 Solving hydrodynamics

The hydrodynamical equations can be discretized in different ways employing Lagrangian, Eulerian, or arbitrary Lagrange-Eulerian techniques. The Lagrangian specification of the field assumes an observer that follows an individual fluid parcel, with its own properties like density, as it moves through space and time. The Eulerian specification focuses on specific locations in space through which the fluid flows as time passes. In addition, numerical approaches also employ mesh-free or mesh-based algorithms.

The hydrodynamical equations have to be complemented by various astrophysical processes that shape the galaxy population. Most of these processes are implemented through effective, so-called sub-resolution models, which are necessary due to the limited numerical resolution of simulations. These processes, depending on the simulation, can include gas cooling, interstellar medium, star formation, stellar feedback, seeding and growth of supermassive black holes (SMBHs), AGN feedback, magnetic fields, cosmic rays, radiation

## 1.5 The simulations of galaxy groups of this thesis

hydrodynamics, dust physics, thermal conduction, and viscosity.

## 1.5 The simulations of galaxy groups of this thesis

We consider the following three cosmological simulations to study galaxy groups in this thesis, with their basic properties shown in Table 1.2.

Simulation	Dark matter particle mass ( $M_\odot$ )	Mean gas particle/cell mass ( $M_\odot$ )	Box size <sup>(a)</sup> (cMpc)	Code	Hydro scheme
TNG100	$7.5 \times 10^6$	$1.4 \times 10^6$	110.7	AREPO	Moving Mesh
SIMBA	$9.6 \times 10^7$	$1.8 \times 10^7$	147.6	GIZMO	Meshless Finite Mass
EAGLE	$9.7 \times 10^6$	$1.8 \times 10^6$	100.0	GADGET3	Modern SPH

**Table 1.2.** The properties of the simulations used in this thesis.

(a) Side length of the cubic box in comoving Mpc.

### 1.5.1 IllustrisTNG

IllustrisTNG<sup>1</sup> ([Pil+18]) is a suite of large-volume cosmological galaxy formation simulations which present the next generation of the Illustris simulation ([Vog+14]). Based on the moving-mesh AREPO code ([Spr10]), IllustrisTNG solves the equations of gravity and magneto-hydrodynamics([PBS11]) and models the formation and evolution of galaxies on cosmological scales. It includes a comprehensive physical model for galaxy formation, including radiative cooling of gas, the formation of stars from the cold gas, stellar evolution, stellar feedback ([Pil+18]), and physical processes relevant to SMBHs, including seeding, merging, and feedback ([Wei+17]). In this thesis, we use from the suite, the periodic box with side length of 100 Mpc (TNG100). The calibration of the free parameters of the TNG model was carried out at the fiducial TNG100 resolution by comparing against several observables of the galaxy population.

---

<sup>1</sup><https://www.tng-project.org/>

### 1.5.2 SIMBA

The SIMBA hydrodynamical simulations<sup>2</sup> ([Dav+19]) update the physics of the MUFASA simulation ([DTH16]) to simulate galaxy formation on cosmological scales. SIMBA implements its physical processes on top of the GIZMO code ([Hop15]), which employs a meshless finite mass (MFM) hydrodynamics method. Similar to IllustrisTNG, SIMBA implements models for key relevant physical processes such as gas cooling, star formation, stellar feedback, black hole formation and growth, and AGN feedback. The SIMBA model has been used to run several simulations with different resolutions and box sizes. In this work, we exclusively use the highest resolution box of the 150 Mpc side length.

### 1.5.3 EAGLE

The EAGLE simulation<sup>3</sup> model ([Cra+15]; [Sch+15b]) uses a modified version of the GADGET-3 smoothed particle hydrodynamics (SPH) code ([Spr05]; [Sch+15a]) to perform galaxy formation simulations on cosmological scale boxes. In addition to solving the equations of gravity and hydrodynamics, EAGLE implements several physical processes relevant to galaxy evolution. These primarily include gas cooling, star formation, stellar feedback, and SMBH-related processes such as seeding, black hole growth, and AGN feedback. The EAGLE model is calibrated by comparing against observations of galaxy stellar mass function, the central galaxy stellar to black hole mass relation, and galaxy sizes. We exclusively use the highest resolution 100 Mpc side-length box of EAGLE.

---

<sup>2</sup><http://simba.roe.ac.uk/>

<sup>3</sup><https://icc.dur.ac.uk/Eagle/>

## 2 Diverse gas properties in groups from different state-of-the-art simulations

Within the galaxy group mass range selected ( $10^{13} - 10^{14} M_{\odot}$ ), we have 168, 344, and 155 halos from TNG100, SIMBA, and EAGLE, respectively. All the analysis is performed on these halos. We can draw statistical inferences about the overall population with these data points.

### 2.1 Total gas properties in halos

In this section, we look at the gas content in the halos of each simulation. We calculate the gas mass( $M_{gas}$ ) by adding all the mass in gas cells within  $r_{200c}$  of each halo, and the total mass ( $M_{200c}$ ) by adding all the mass in the gas cells, dark matter particles, star particles, and black hole particles within  $r_{200c}$  of the halo. Then the gas fraction  $f_g$  is the ratio of the  $M_{gas}$  over  $M_{200c}$ . We normalise the  $f_g$  with the  $f_{b,cosmic}$  to compare the gas with the cosmic average baryon fraction.

## 2.1 Total gas properties in halos

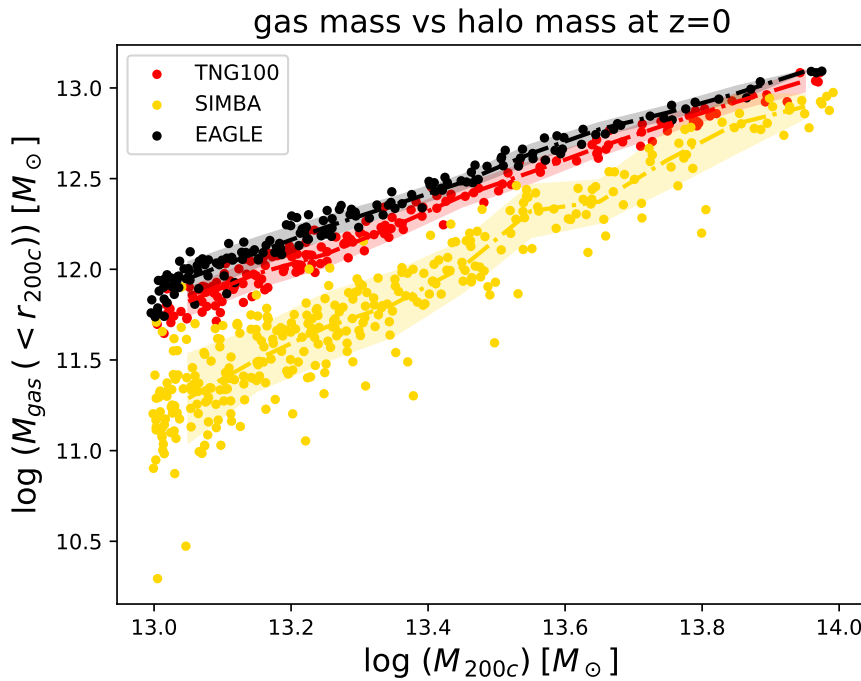


**Figure 2.1.** Distribution of the gas mass as a function of the total halo mass. Solid dots represent the individual halos, dashed-dotted lines represent the running median values in bins of 0.1 dex, and the shaded region is the  $1 - \sigma$  deviation.

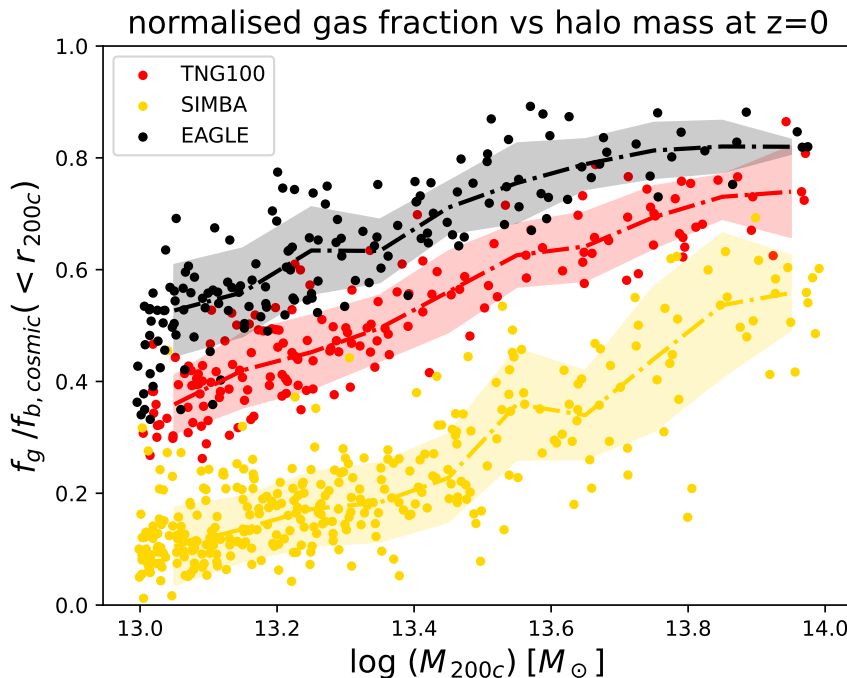


**Figure 2.2.** Comparison of the  $f_g - M$  relation in the three simulations. Solid dots represent the individual halos, dashed-dotted lines represent the running median values in bins of 0.1 dex, and the shaded region is the  $1 - \sigma$  deviation.

## 2.1 Total gas properties in halos

Comparing the trends in the simulations, we find that the  $M_{gas}$  (Figure 2.1) and the  $f_g/f_{b,cosmic}$  (Figure 2.2) in the halos are much lower for SIMBA as compared to TNG100 and EAGLE, for the entire halo mass range. EAGLE has the highest median values for both  $M_{gas}$  and normalised  $f_g$  throughout the halo mass range. We check for the basic differences in the simulations that might cause the variation in the baryon distribution. With similar box volumes (Table 1.2) and hence, a similar halo count on a statistical level, we check for the resolution variation by looking at the different resolution runs of TNG100, namely TNG100-2, and TNG100-3, with baryonic resolution of  $1.1 \times 10^7 M_\odot$ , and  $8.9 \times 10^7 M_\odot$  respectively. We find that the resolution does not affect the  $f_g/f_{b,cosmic}$  (Figure 2.3). This means that in SIMBA, more gas is driven outside the  $r_{200c}$  by feedback processes as compared to TNG100 and EAGLE. This has been shown in [ANP23]; [Wri+24].

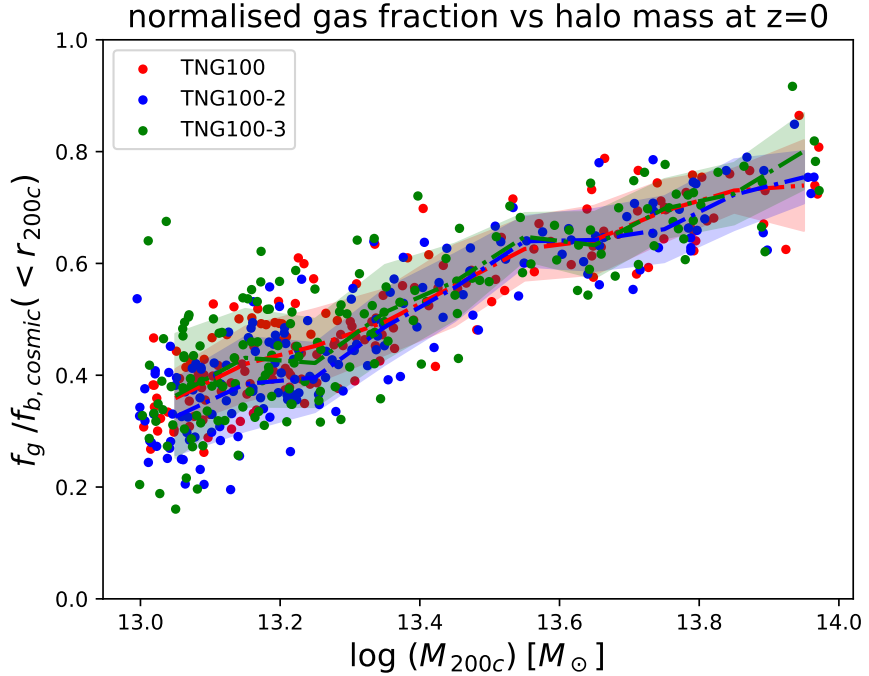


**Figure 2.3.** Comparison of the  $f_g - M$  relation in the three resolutions of TNG100. Solid dots represent the individual halos, dashed-dotted lines represent the running median values in bins of 0.1 dex, and the shaded region is the  $1 - \sigma$  deviation.

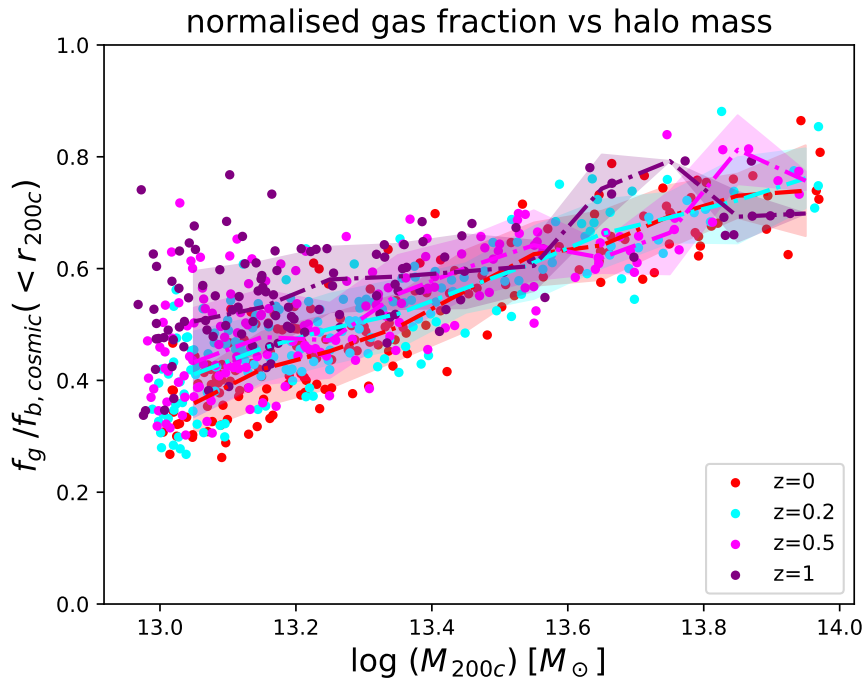


**Figure 2.4.** Comparing the  $f_g - M$  relation in TNG100 plotted at four different redshifts. Solid dots represent the individual halos, dashed-dotted lines represent the running median values in bins of 0.1 dex, and the shaded region is the  $1 - \sigma$  deviation.

We limit our analysis of the gas fraction to  $z = 0$ . While observational surveys in X-ray detect groups at different redshifts, we are justified in limiting our analysis as the  $f_g - M$  relation does not show significant divergence for the four different redshift values being compared in TNG100 (Figure 2.4).

## 2.2 Radial gas profiles

In this section, we compare the radial distribution of the gas content (Figure 2.5, Figure 2.6, Figure 2.7) in the three simulations and make the same resolution checks as above to see if different resolutions affect the profiles. We again find similar trends as for the total gas content when comparing the three simulations with overlap between the TNG100 and EAGLE populations. We also find that the resolution does not affect the radial distribution of the gas (Figure 2.8).

## 2.2 Radial gas profiles

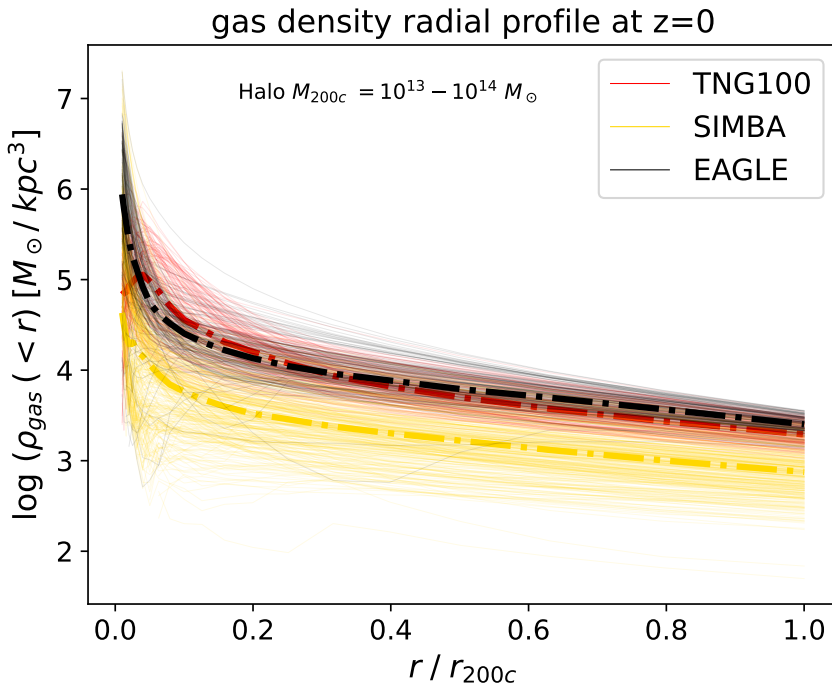


**Figure 2.5.** Gas density radial profiles in the three simulations. The solid curves show the profiles for each halo and the dash-dotted curve shows the running median in bins of 0.1 dex from  $0.01r_{200c}$  to  $1r_{200c}$ .

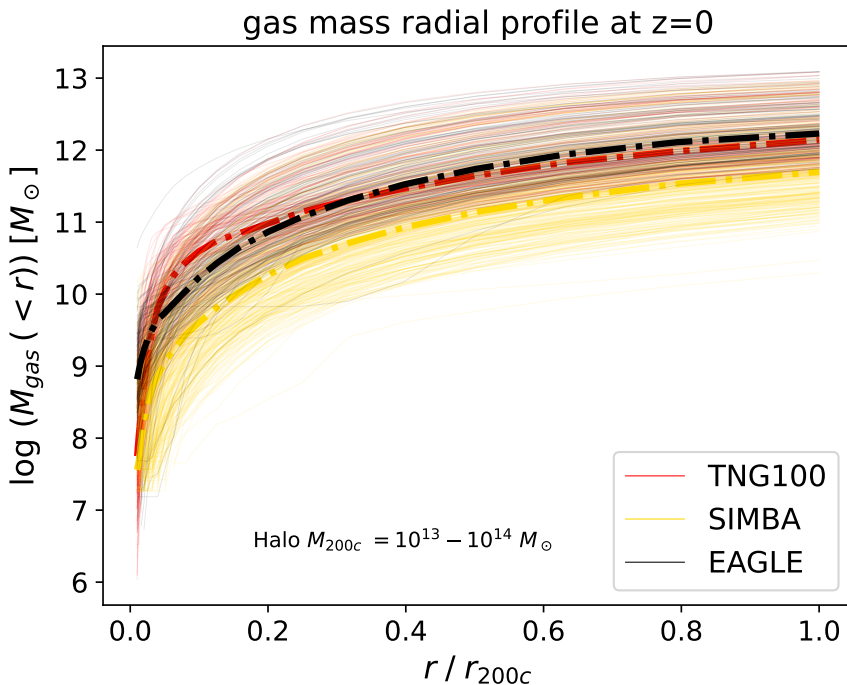


**Figure 2.6.** Gas mass radial profiles in the three simulations. The solid curves show the profiles for each halo and the dash-dotted curve shows the running median in bins of 0.1 dex from  $0.01r_{200c}$  to  $1r_{200c}$ .

## 2.2 Radial gas profiles

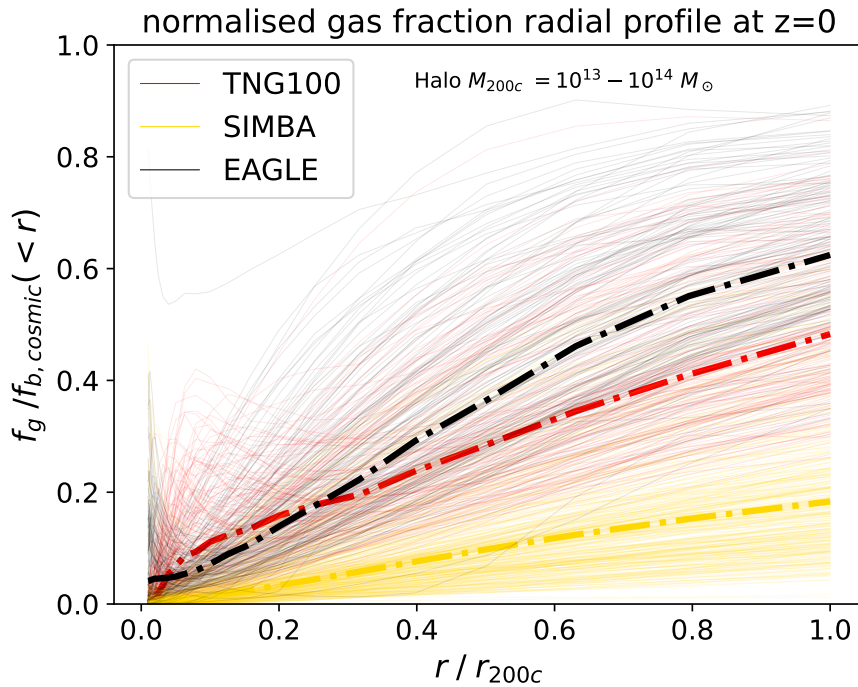


**Figure 2.7.** Normalised gas fraction radial profiles in the three simulations. The solid curves show the profiles for each halo and the dash-dotted curve shows the running median in bins of 0.1 dex from  $0.01r_{200c}$  to  $1r_{200c}$ .

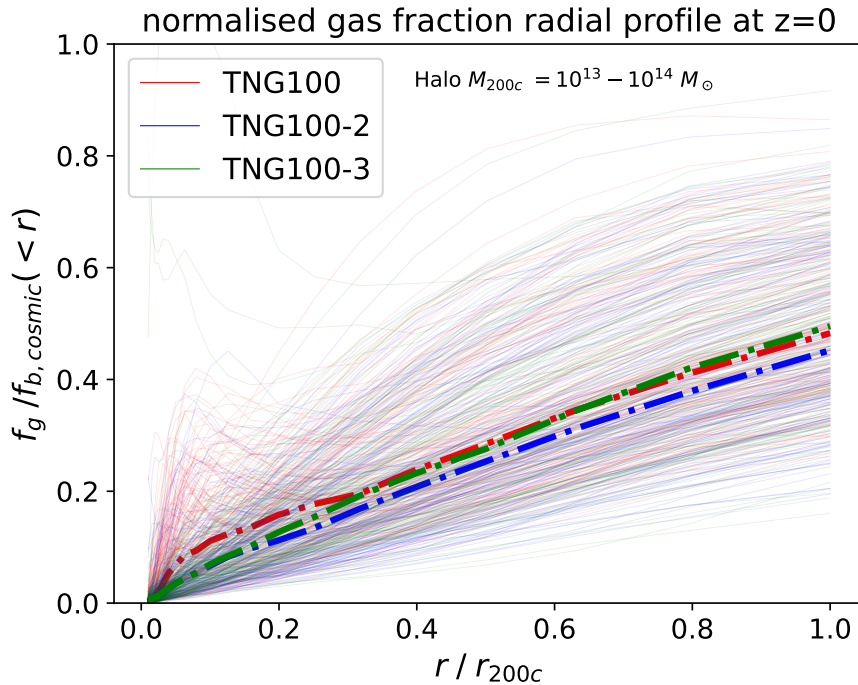


**Figure 2.8.** Normalised gas fraction radial profiles in the three resolutions of TNG100. The solid curves show the profiles for each halo and the dash-dotted curve shows the running median in bins of 0.1 dex from  $0.01r_{200c}$  to  $1r_{200c}$ .

## 2.3 Intrinsic X-ray luminosity

Having looked at the gas content directly obtained from the simulation data, we now move a step further and look at an observable quantity, namely, the X-ray luminosity ( $L_x$ ), computed from the simulation data.

Intrinsic X-ray emission of the diffuse gas is computed for non-star-forming gas cells by assuming an emission model APEC ([Smi+01]) from the XSPEC package<sup>1</sup> using the element abundances traced by simulations, which is practically done by implementing the VAPEC model in the XSPEC package. This emission is stored as X-ray cooling rates for broad-band emission in the soft X-ray band of 0.5-2 keV and for narrow bands at 9 specific lines: CV (298.97 eV), CVI (367.47 eV), NVI (419.86 eV), NVII (500.36 eV), OVIIIf (560.98 eV), OVIIIr (573.95 eV), OVIII (653.49 eV), FeXVII (725.05 eV), and NeX (1021.5 eV).

X-ray luminosity of each gas cell is then computed as:

$$L_x[\text{erg/s}] = \text{cooling rate}[\text{erg cm}^3/\text{s}] * n_e[\text{cm}^{-3}] * n_h[\text{cm}^{-3}] * V[\text{cm}^3]$$

where  $n_h$  and  $n_e$  are hydrogen and electron number densities respectively, and  $V$  is the volume of the gas cell.

---

<sup>1</sup><https://heasarc.gsfc.nasa.gov/xanadu/xspec/>

### 2.3 Intrinsic X-ray luminosity

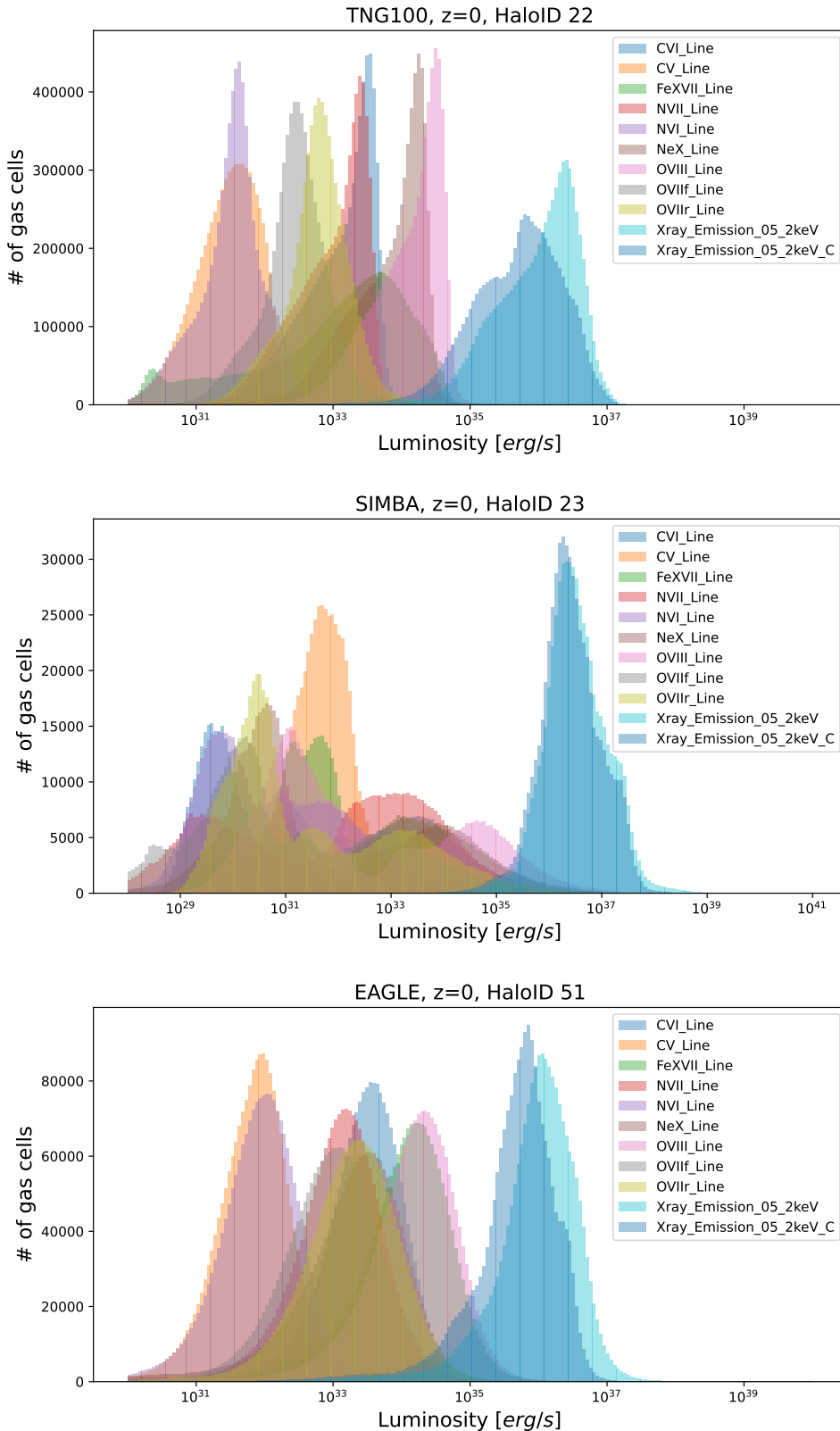


**Figure 2.9.** Contribution of the continuum and line emission to the total X-ray emission for selected HaloIDs from each simulation

### 2.3 Intrinsic X-ray luminosity

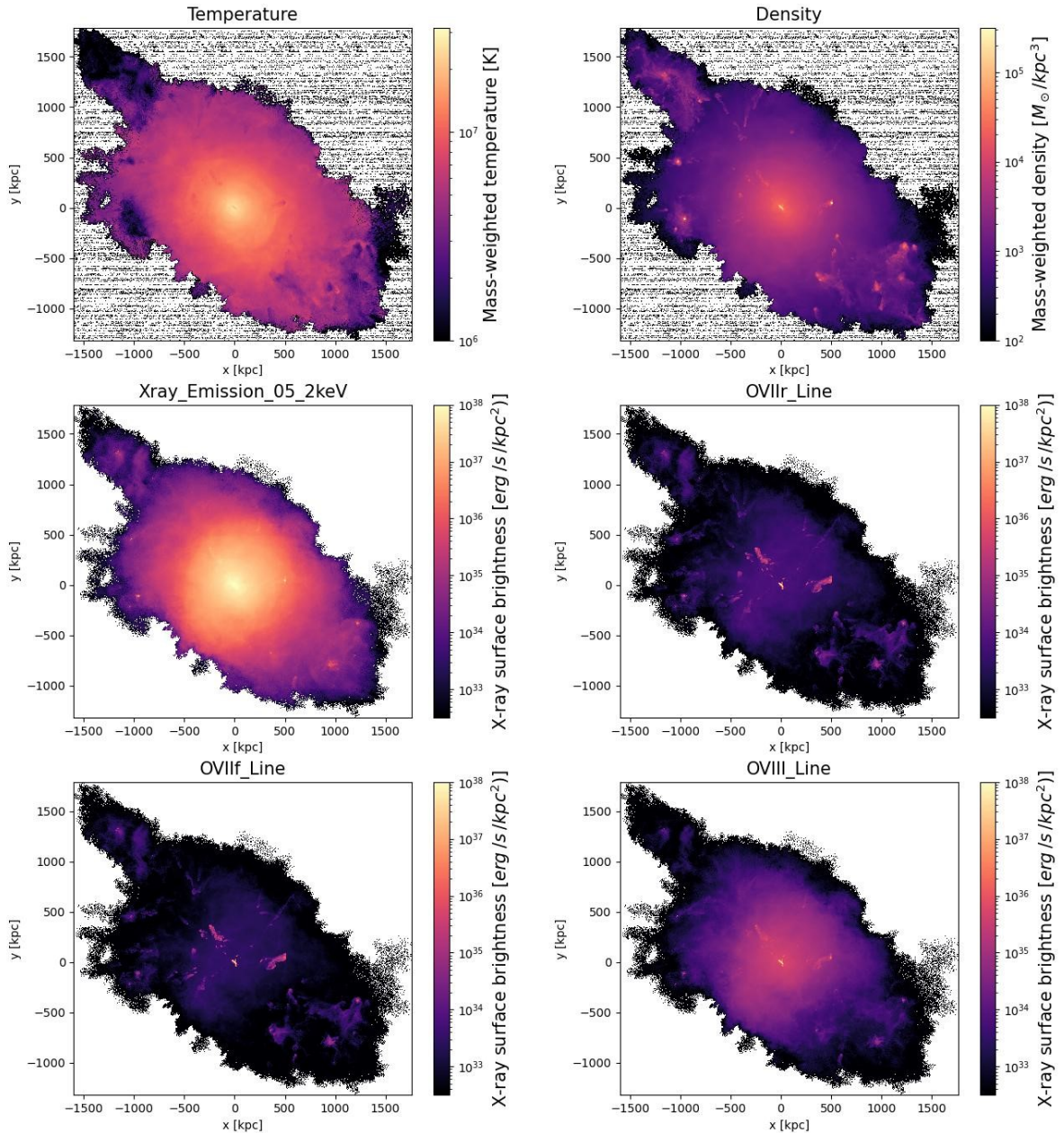


**Figure 2.10.** Temperature, density, and X-ray surface brightness maps of HaloID 22 in TNG100 at  $z=0$

### 2.3 Intrinsic X-ray luminosity

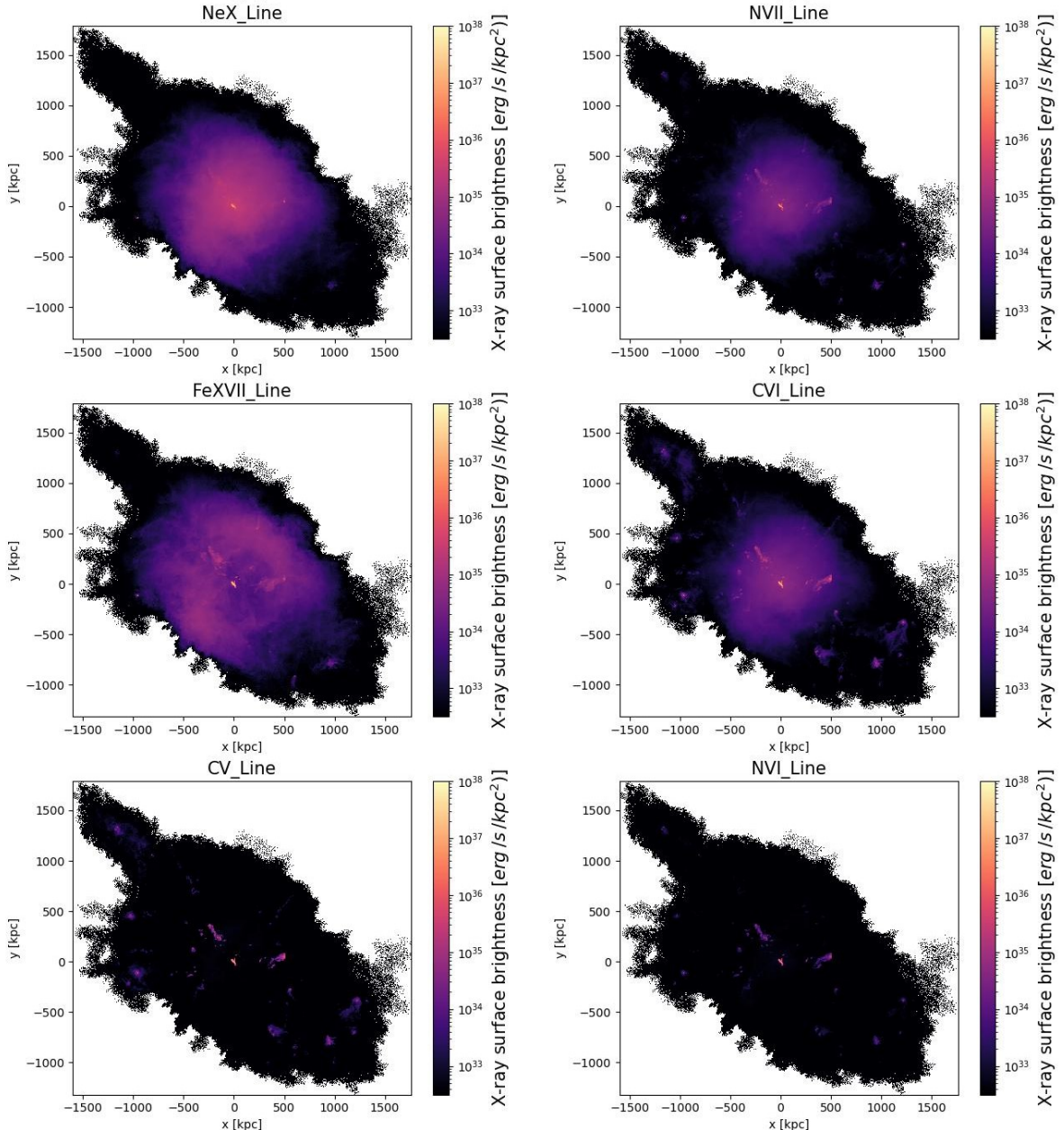


**Figure 2.11.** X-ray surface brightness maps of HaloID 22 in TNG100 at  $z=0$

A major contribution to the X-ray luminosity is seen from the soft band continuum emission. This is shown for individual haloIDs in Figure 2.9, Figure 2.10, Figure 2.11. For this thesis, we limit our analysis to the total emission from the soft band, without differentiating the continuum and the line emission.

## 2.4 Differences in the physical models of the simulations that affect the gas distribution in groups

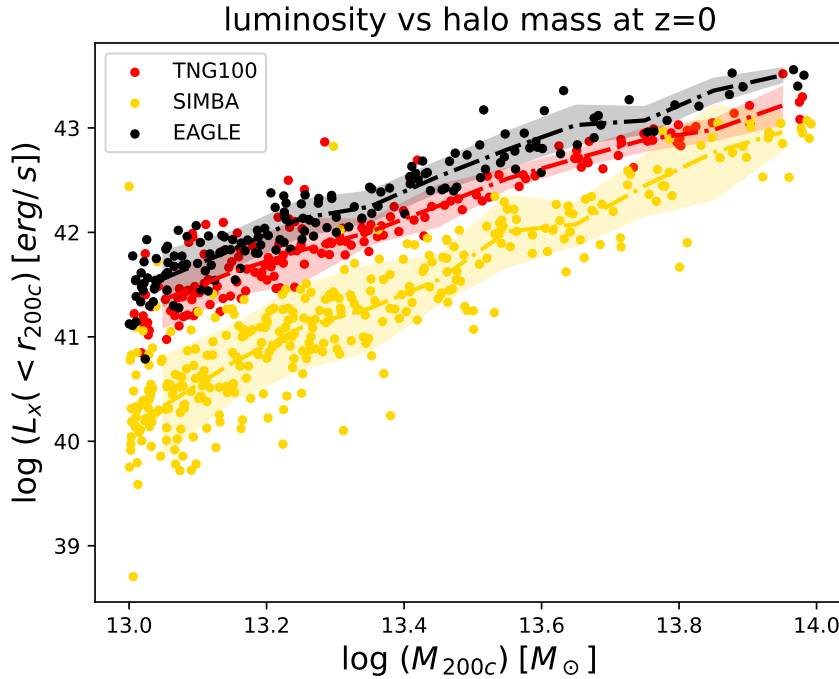


**Figure 2.12.** Comparing the intrinsic  $L_x - M$  relation of each simulation. Solid dots represent individual halos, dashed-dotted lines represent the running median values in bins of 0.1 dex, and the shaded region is the  $1 - \sigma$  deviation.

The calculated intrinsic luminosity shows the same trend as the gas properties, with EAGLE having the highest median luminosity for the entire mass range. EAGLE and TNG100 show an overlap in the  $1 - \sigma$  range at varying mass bins, while SIMBA has a consistently low luminosity with little overlap only at the high-mass end as shown in Figure 2.12.

## 2.4 Differences in the physical models of the simulations that affect the gas distribution in groups

As discussed in Chapter 1, the hydrodynamic equations are complemented by various astrophysical processes, due to the limit in numerical resolution. The dominant physical process reshaping the gas/baryon distribution ([Wri+24] in the galaxy group mass regime is AGN feedback ([ANP23]; [Sor+22]). In this section, we discuss the model differences in SMBH seeding, growth and mergers, and AGN feedback in the three simulations.

The three simulations take somewhat similar approaches for seeding SMBHs in haloes. They run a halo finder algorithm on the fly and place an SMBH with a constant mass in the halo whenever the halo mass (IllustrisTNG and EAGLE) or stellar mass (SIMBA) exceeds

## 2.4 Differences in the physical models of the simulations that affect the gas distribution in groups

a specific value. In all three models, SMBH growth then occurs through the accretion of matter and mergers with other SMBHs. In IllustrisTNG, accretion is modeled using the Bondi accretion rate ([Bon52]; [BH44]), which depends on SMBH mass, the local density, temperature, and the SMBH velocity relative to its local gas. EAGLE employs a modified Bondi accretion rate that accounts for the angular momentum of the gas around the SMBH ([Ros+15]). In SIMBA, accretion proceeds through two different channels, based on the gas temperature. Bondi accretion occurs for the warm–hot non-ISM (InterStellar Medium) gas ( $T > 10^5 K$ ), while the cold gas accretes based on a torque-limited model, derived from the gravitational instabilities of the gaseous disc ([HQ11]; [Ang+17]).

Description of the AGN feedback (see also Table 2.1):

(i) IllustrisTNG: Depending on the accretion rate, SMBH feedback operates in one of two modes: thermal or kinetic. These two modes do not operate simultaneously. When in thermal mode, thermal energy from the SMBH feedback is injected (continuous in time) into the gas cells in the local environment of the SMBH. This mode of AGN feedback increases the temperature of these gas cells and affects their evolution. When the accretion rate onto the SMBH is low, which is typically the case for more massive halos, the feedback switches to a kinetic mode, where it injects momentum and kinetic energy into surrounding gas cells. This energy injection, which is released in discrete events, is imparted at random orientations and is isotropic when time-averaged. However, it can result in non-isotropic large-scale outflows depending on the physical conditions of the gas in the vicinity of the SMBH ([Wei+17]; [Nel+19]; [Pil+21]). The impact of these outflows on the distribution of gas out to large scales is presented in [ANP23]. Finally, in addition to these two distinct feedback modes, the TNG model also includes an AGN radiative feedback channel that operates during the radiatively efficient state (i.e. thermal mode), impacting the temperature and cooling rate of halo gas particularly at high luminosities.

(ii) SIMBA: AGN feedback operates in one of three modes: two kinetic wind modes, referred to as ‘radiative AGN winds’ and ‘jet mode’ and one ‘X-ray’ mode. The choice of the mode depends on the SMBH mass and accretion rate in Eddington units. In the kinetic modes, AGN feedback is implemented by probabilistically kicking individual gas particles with a high velocity that depends on the accretion rate. At high accretion rates (radiative mode feedback), the injected wind particle speed is  $10^3 km/s$ , whereas at low accretion rates(jet mode feedback) this speed increases substantially, up to  $10^4 km/s$ . These outflows are bipolar at injection, with orientation parallel to the angular momentum of the surrounding baryonic medium. When the jet mode of AGN feedback is active and the galaxy gas to stellar mass ratio is below 20 percent, an X-ray feedback mode also becomes active. Finally, at high accretion rates, kicked gas is unheated and keeps its ISM temperature, while for the jet mode, kicked gas is also heated to the halo virial

## *2.4 Differences in the physical models of the simulations that affect the gas distribution in groups*

temperature. In both cases, AGN-driven wind particles are hydrodynamically decoupled for some time, which is not the case for either IllustrisTNG or EAGLE. All energy injection is continuous in time.

(iii) EAGLE: AGN feedback has only one mode, which is thermal, and is implemented as an injection of thermal energy. The energy from AGN feedback is proportional to the accretion rate onto the SMBH. This energy is injected stochastically by increasing the temperature of the gas particles around the SMBH by 108.5 K. This high temperature is designed to prevent numerical overcooling that would otherwise occur at lower temperatures.

2.4 Differences in the physical models of the simulations that affect the gas distribution in groups

IllustrisTNG			
$\dot{M}_{accr}$	Mode	Energy	Details
$\dot{\mathbf{M}}_{Bondi}$	Thermal ( $< \chi$ )	$\Delta\dot{E} = \epsilon_{f,high}\epsilon_r \dot{M}_{BH}c^2$ $\epsilon_{f,high} = 0.1, \epsilon_r = 0.2$	Thermal injection in feedback region.
	Kinetic ( $> \chi$ )	$\Delta\dot{E} = \epsilon_{f,kin}\dot{M}_{BH}c^2$ $\epsilon_{f,kin} = \min\left(\frac{\rho}{0.05\rho_{SFT}}, 0.2\right)$	Momentum boost. $p_{inj} = \sum m_j \sqrt{\frac{2\Delta E \omega(\mathbf{r})}{\rho}} \mathbf{n}$
SIMBA			
$\dot{M}_{accr}$	Mode	Details	
$\dot{\mathbf{M}}_{Torque} + \dot{\mathbf{M}}_{Bondi}$	Kinetic winds	Outflow velocity: $v_{w,EL} = 500 + 500 (\log M_{BH} - 6) / 3 \text{ km s}^{-1}$ . No temperature modification (ejected at ISM temperature)	
	Kinetic jets	Outflow velocity: $v_{w,jet} = v_{w,EL} + 7000 \log(0.2/f_{Edd}) \text{ km s}^{-1}$ (cap to the increase at 7000 $\text{km s}^{-1}$ ). Only occurs with $M_{BH} > 10^{7.5} M_\odot$	
	X-ray heating	When jet mode is active, x-ray heating is applied, given that $f_{gas} (= M_{gas}/M_*) < 0.2$ $\dot{E}$ depends on $\dot{M}_{accr}$ , $\sim (1/r^2)$ , temperature of gas, proton density. Half added as an outward momentum kick, half added as thermal energy.	
EAGLE			
$\dot{M}_{accr}$	Mode	Energy	Details
$\dot{\mathbf{M}}_{Bondi} \times \min\left(\frac{(c_s/V_\phi)^3}{C_{visc}}, 1\right)$	Thermal	$\Delta\dot{E} = \epsilon_f \epsilon_r \dot{M}_{accr} c^2$ $\epsilon_f = 0.15, \epsilon_r = 0.1$	Thermal addition to the reservoir. $\Delta T_{AGN} = 10^{8.5} K$

**Table 2.1.** Details of the AGN feedback models for the simulations

# 3 From simulated data to X-ray observations of galaxy groups

To reach meaningful conclusions about the underlying physics affecting the gas properties in galaxy groups, we need to bridge theory, i.e. the intrinsic data obtained from the simulations with observations of galaxy groups. As the observational study of galaxy groups in X-ray is prone to biases, influenced by data quality and instrumental effects, we need to include a layer of observational realism for their identification in simulated groups/halos. To do this, we can build a pipeline going from the intrinsic simulation data - to the intrinsic observable quantity - to the mocked observed quantity. The analysis performed on the mocked observable to make inferences will then provide an apples-to-apples comparison with the observational inferences.

In this work, we build a part of this pipeline and look to draw some conclusions, which can then be furthered by completing the pipeline. The following sections explain the mocking process.

## 3.1 Simulated data to intrinsic observable

We begin by loading the data of an individual halo from the simulation and creating a file to store the data loaded. Using the `yt` package<sup>1</sup>, we load this stored file again and add filters to select hot gas ( $> 10^5$  K).

Next, we set up the configuration for the source model for X-ray emission in the `pyXSIM` package<sup>2</sup>. We choose the 'CIESourcemodel' (creates a Collisional Ionization Equilibrium spectrum, using the APEC model ([Smi+01]) ). We set the energy range to 0.05 - 4.0 keV so that it covers the soft X-ray band of 0.5 - 2 keV used to calculate the luminosity. Figure 3.1 shows an example code snippet for the aforementioned procedure.

---

<sup>1</sup><https://yt-project.org/>

<sup>2</sup><https://hea-www.cfa.harvard.edu/jzuhone/pyxsim/>

### 3.1 Simulated data to intrinsic observable

```

# Loading the halo, particle, header data
halo = il.groupcat.loadSingle(basePath, snap, haloID=haloID)
gas = il.snapshot.loadHalo(basePath, snap, haloID, 'gas')
header = il.groupcat.loadHeader(basePath, snap)
h = header["HubbleParam"]

# Loading the mass table
with h5py.File(il.snapshot.snapPath(basePath, snap), 'r') as f:
    header_snap = dict(f['Header'].attrs)

# writing an HDF5 file to store the loaded data for yt use
filename = "../mockhalo_%s_%d.hdf5" %(sim,haloID)

with h5py.File(filename, 'w') as f:
    for key in gas.keys():
        f['PartType0/' + key] = gas[key]

    # some metadata that yt demands
    f.create_group('Header')
    f['Header'].attrs['NumFilesPerSnapshot'] = 1
    f['Header'].attrs['MassTable'] = header_snap['MassTable']
    f['Header'].attrs['BoxSize'] = header['BoxSize']
    f['Header'].attrs['Time'] = header['Time']
    f['Header'].attrs['NumPart_ThisFile'] = np.array([gas['count'],0,0,0,0,0])

    # Must have the next six for correct units
    f["Header"].attrs["HubbleParam"] = header["HubbleParam"]
    f["Header"].attrs["Omega0"] = header["Omega0"]
    f["Header"].attrs["OmegaLambda"] = header["OmegaLambda"]

    # These correspond to the values from the TNG simulations
    f["Header"].attrs["UnitLength_in_cm"] = header_snap['UnitLength_in_cm']
    f["Header"].attrs["UnitMass_in_g"] = header_snap['UnitMass_in_g']
    f["Header"].attrs["UnitVelocity_in_cm_per_s"] = header_snap['UnitVelocity_in_cm_per_s']

# Load yt dataset
ds = yt.load(filename)

# define and add a hotgas filter to the dataset
def hot_gas(pfilter, data):
    pfilter1 = data[pfilter.filtered_type, "temperature"] > 10**5 # K
    pfilter2 = data["PartType0", "StarFormationRate"] == 0.0
    pfilter3 = data["PartType0", "GFM_CoolingRate"] < 0.0
    return (pfilter1 & pfilter2) & pfilter3

yt.add_particle_filter("hot_gas", function=hot_gas, filtered_type='gas',
                      requires=["temperature", "density"])
ds.add_particle_filter("hot_gas")

# set the source model to simulate the source
nbins = 4000
source_model = pyxsim.CIESourceModel("apec", emin, emax, nbins, ("hot_gas", "metallicity"),
                                     temperature_field=("hot_gas", "temperature"),
                                     emission_measure_field=("hot_gas", "emission_measure"))

```

**Figure 3.1.** Example code snippet for loading the simulation data and configuring the source emission model.

## 3.2 Creating ideal mocks

Having the source model set up, we specify fiducial values of the exposure time, collecting area, and redshift of the halo. These values must be higher than the ones for the actual telescope instrument. This is done so that we have more sample photons in the ideal mock than the telescope will finally detect. We choose the exposure time to be 1000 ks, the collecting area to be 5000 cm<sup>2</sup>, and the redshift of the halos to be 0.025. Then we create a square box centered at our source halo, which will be used to draw the gas cells/particles to make the photons. The side length of this box is chosen to be  $2 * r_{200c}$  of the halo. Then, using pyXSIM, we make the photons and project them in a random direction (along the x-axis of the simulation box), including the foreground absorption ('wabs' model with foreground column density nH= 10<sup>20</sup> cm<sup>-2</sup>). We store the catalog of the photon events in a 'SIMPUT' format for further processing. Figure 3.2 shows an example code snippet for the aforementioned procedure.

```
# defining the source redshift, the center and size of the simulated box
redshift = 0.025
box_size = halo['Group_R_Crit200']/h *10**-3 # Mpc
c = ds.arr([halo["GroupPos"][0], halo["GroupPos"][1], halo["GroupPos"][2]],
           "code_length")
width = ds.quan(box_size, "Mpc")
le = c - width
re = c + width
box = ds.box(le, re)

# generating and projecting the photons and writing to simput
n_photons, n_cells = pyxsim.make_photons(photon_file, box, redshift,
                                           (area, 'cm**2'), (exp_time, 'ks'),
                                           source_model)

n_events_x = pyxsim.project_photons(photon_file, events_file_x, "x",
                                      (45., 30.), absorb_model="wabs",
                                      nH=0.01)

events_x = pyxsim.EventList(events_file_x + '.h5')
events_x.write_to_simput(simput_file_x, overwrite=True)
```

**Figure 3.2.** Example code snippet for creating the box, generating and projecting photons, and storing them. The values for the variables in the code are mentioned in the section above.

At this point, we have created a photon event catalog corresponding to an ideal mock observation of an object situated at a redshift of 0.025 based on an ideal telescope with the configuration of 1000 ks exposure time, 5000 cm<sup>2</sup> of collecting area, and photon detection

### 3.3 Creating Chandra mocks

in the energy range of 0.05 - 4.0 keV. This catalog can now be used to create mocks for any observational surveys with suitable instrumental configurations.

## 3.3 Creating Chandra mocks

We make the Chandra mock observation by using the **SOXS** package<sup>3</sup>. The mocks we create are for the Chandra ACIS I instrument. More specifically, mock event files are produced by projecting the photons onto a detector plane and convolving them with an instrument model for the ACIS I detector, using instrumental specifications of Cycle 22. We choose an exposure time of 100 ks, as it is in the range of the exposure times used for observing groups and clusters with Chandra ([Sun+09]). Since Chandra has a small FoV of 17 arcmin, we change the instrument details in the SOXS instrument registry such that the FoV is adjusted for each observation, and it is set to be  $2 * r_{200c}$  of the halo. This ensures that the entire halo (within  $r_{200c}$ ) fits inside the observation. The mocks used for this analysis are created without including background photons. Figure 3.3 shows an example code snippet for using SOXS to create the Chandra mocks.

```
#Load the instrument with the new FoV
instrument = Chandra_instrument(sim, basePath, snap, haloID)

#simulate the observation without adding background
sky_center = (45.0, 30.0)
soxs.instrument_simulator(input_file, output_file, (100, 'ks'), instrument, sky_center,
                           overwrite=True, instr_bkgnd=False, foreground=False, ptsrc_bkgnd=False)
```

**Figure 3.3.** Example code snippet for creating Chandra mocks using SOXS without background.

## 3.4 Creating XMM-Newton and eROSITA mocks

To create the mock observations for XMM-Newton and eROSITA, we use the **SIXTE** package<sup>4</sup> ([Dau+19]). Figure 3.4 shows an example to run the 'runsixt' command for eROSITA with an exposure time of 600 seconds, where the XML file contains the instrument specifications, the Simput takes the ideal mock previously created as input, and EvtFile is the output event file for the mock observation.

<sup>3</sup><https://hea-www.cfa.harvard.edu/soxs/index.html>

<sup>4</sup><https://www.sternwarte.uni-erlangen.de/sixte/>

```
# Run the SIXTE command
$SIXTE/bin/runsixt \
    XMLFile=${xml} \
    RA=45.000 Dec=30.000 \
    Prefix="" \
    Simput=${simput} \
    EvtFile=${base} \
    Exposure=600 \
    background=no \
    clobber=yes
```

**Figure 3.4.** Example code snippet for running the SIXTE package to create mocks without background

For XMM-Newton mocks, we choose the EPIC-pn detector [Str+01] with the thin filter. We change the FoV of the detector to  $1^\circ$  so that the halo with the largest  $r_{200c}$  can fit in the detection. We choose an exposure time of 10 ks, corresponding to the average effective exposure of the XMM-Newton XXL survey ([Ada+18]), and we do not include background photons in the mock.

For eROSITA mocks, we iterate the 'runsixt' command for all seven telescope modules of eROSITA. The exposure time is set to 1.2 ks, corresponding to the eFEDS average exposure ([Liu+22]), which also lies in the eRASS1 range of exposure time ([Bul+24]), and no background photons are added to the mock.

### 3.4.1 Notes

- During the mocking process, HaloID '20' in the EAGLE simulation, which is a part of the sample of halos with  $10^{13}M_\odot < M_{200c} < 10^{14}M_\odot$ , was excluded from the sample due to a computation time issue in the SIXTE package. So, we have excluded this halo from our analysis from now on. This means we now have 154 halos in the EAGLE sample for all further analysis.
- The eROSITA mocks are created for all seven telescope modules (T1 - T7), but because of the light leaks in detectors T5 and T7 ([Pre+21]), we exclude mock data from these two detectors in our analysis.

## 3.5 Calculating X-ray luminosity

The output mock observation files are stored in the 'fits' format, containing the RA, DEC, and energy data of the photons. This data needs to be converted to observable X-ray luminosity to make inferences. We do this as follows:

- We start by loading the output 'fits' file and creating a mask for photon energy in the range of 0.5 - 2 keV.
- We sum the energy of all the photons within this mask, and divide by the exposure time, to get the energy detected per second, or an observed luminosity ( $L_{obs}$ ).
- We divide the  $L_{obs}$  by the telescope collecting area to obtain the X-ray flux. The effective area of the telescope/instrument varies as a function of the photon energy. For simplicity in calculations, we only consider a single value for the entire soft band.
- To obtain the value for Chandra, we use the Chandra ACIS I cycle 22 values downloaded from PIMMS<sup>5</sup>, and find the average value for the soft band. This is found to be 210 cm<sup>2</sup>.
- For XMM-Newton and eROSITA, we use **Engauge Digitizer**<sup>6</sup> to extract data points from the plot in Figure 3.5 and Figure 3.6. We use the data points generated by the digitizer in the soft band and calculate the average value. The average for XMM-Newton EPIC-pn is 1250 cm<sup>2</sup>, and for eROSITA is 2150 cm<sup>2</sup>.
- In the final step, we multiply the flux by the surface area of a sphere, i.e.  $4\pi d_L^2$ , where  $d_L$  is the luminosity distance of the source halo (at the chosen redshift of 0.025), to get the X-ray luminosity of the source halo.

---

<sup>5</sup>[https://cxc.harvard.edu/cgi-bin/prop\\_viewer/build\\_viewer.cgi?ea](https://cxc.harvard.edu/cgi-bin/prop_viewer/build_viewer.cgi?ea)

<sup>6</sup><https://markummitchell.github.io/engauge-digitizer/>

### 3.5 Calculating X-ray luminosity

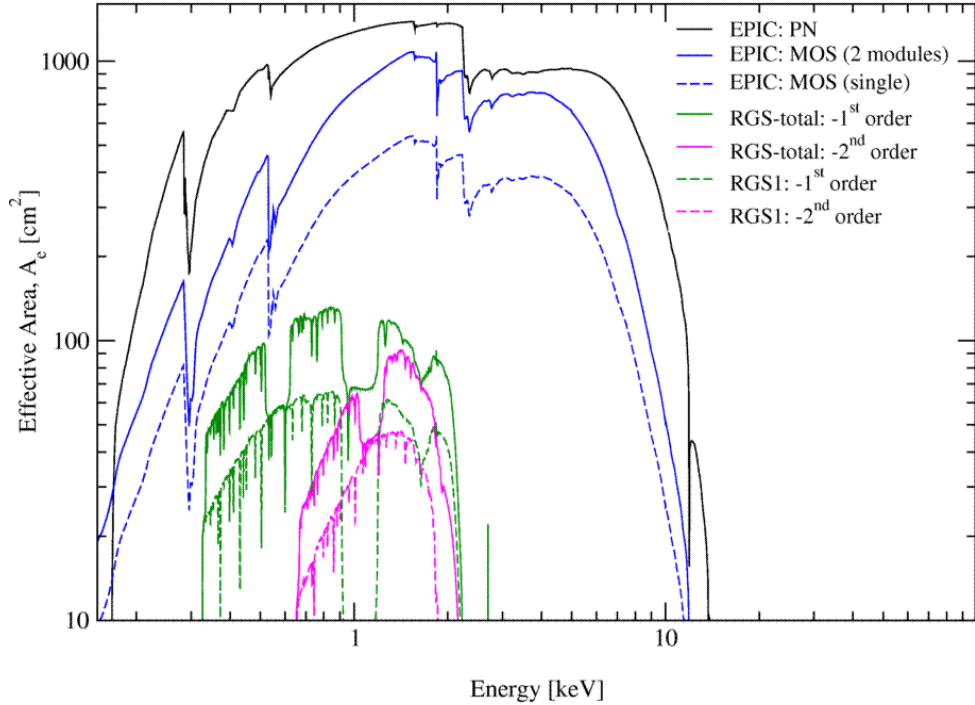


**Figure 3.5.** On-axis effective area of different XMM-Newton instruments. Plot from <sup>7</sup>.

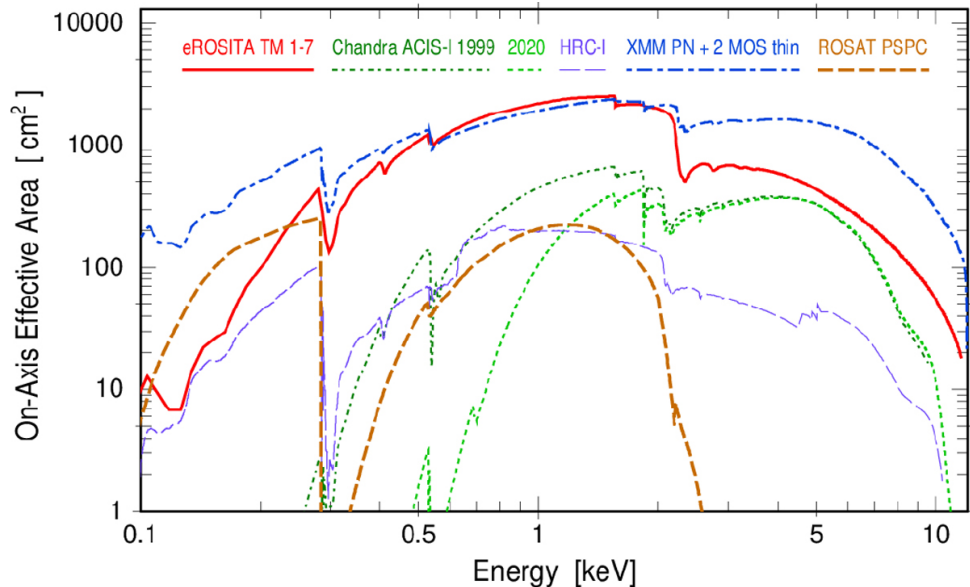


**Figure 3.6.** On-axis effective area of eROSITA compared to other X-ray telescopes. Plot from [Pre+21].

<sup>7</sup>[https://xmm-tools.cosmos.esa.int/external/xmm\\_user\\_support/documentation/uhb/effareaonaxis.html](https://xmm-tools.cosmos.esa.int/external/xmm_user_support/documentation/uhb/effareaonaxis.html)

### 3.5 Calculating X-ray luminosity

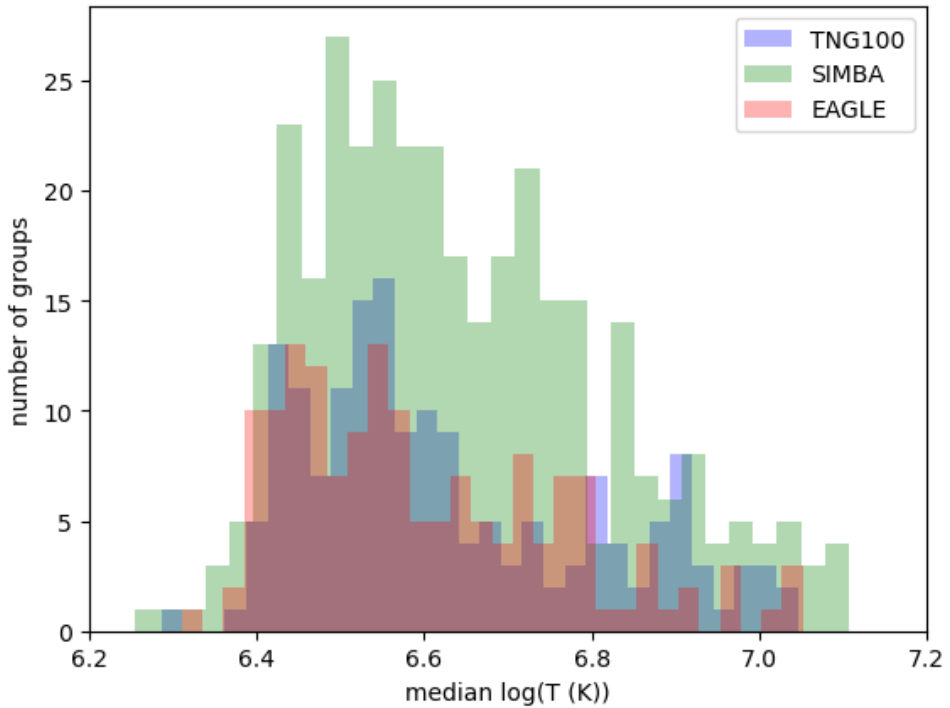


**Figure 3.7.** Histogram showing the distribution of median halo temperature

An alternative method to this process for calculating the luminosity is to count the number of photons in the soft band, divide them by the exposure time to get the count rate, and then use an energy conversion factor (ECF) to convert the count rate into a flux value. This would take into account the energy response of the instrument, but in our case, this method would also involve assuming a single value for the halo temperature, which varies from about  $10^{6.2}$  K to about  $10^{7.1}$  K over the mass range Figure 3.7, to get a single conversion factor for all the halos. It would also involve assuming a single value for the metal abundance in all the halos.

## **4 Observational effects on the inference of the gas content of X-ray detected galaxy groups**

We have now created X-ray mock observations for all three telescopes for each simulation and calculated the X-ray luminosity of each halo. In this chapter, we study how the observational effects, specifically, the detection of a halo affect the intrinsic  $f_g - M$  relation for each simulation (Figure 2.2). First, we look at a sample of the mock observed images for each telescope (Figure 4.1, Figure 4.2, Figure 4.3)

#### 4.1 Chandra mocks

## 4.1 Chandra mocks

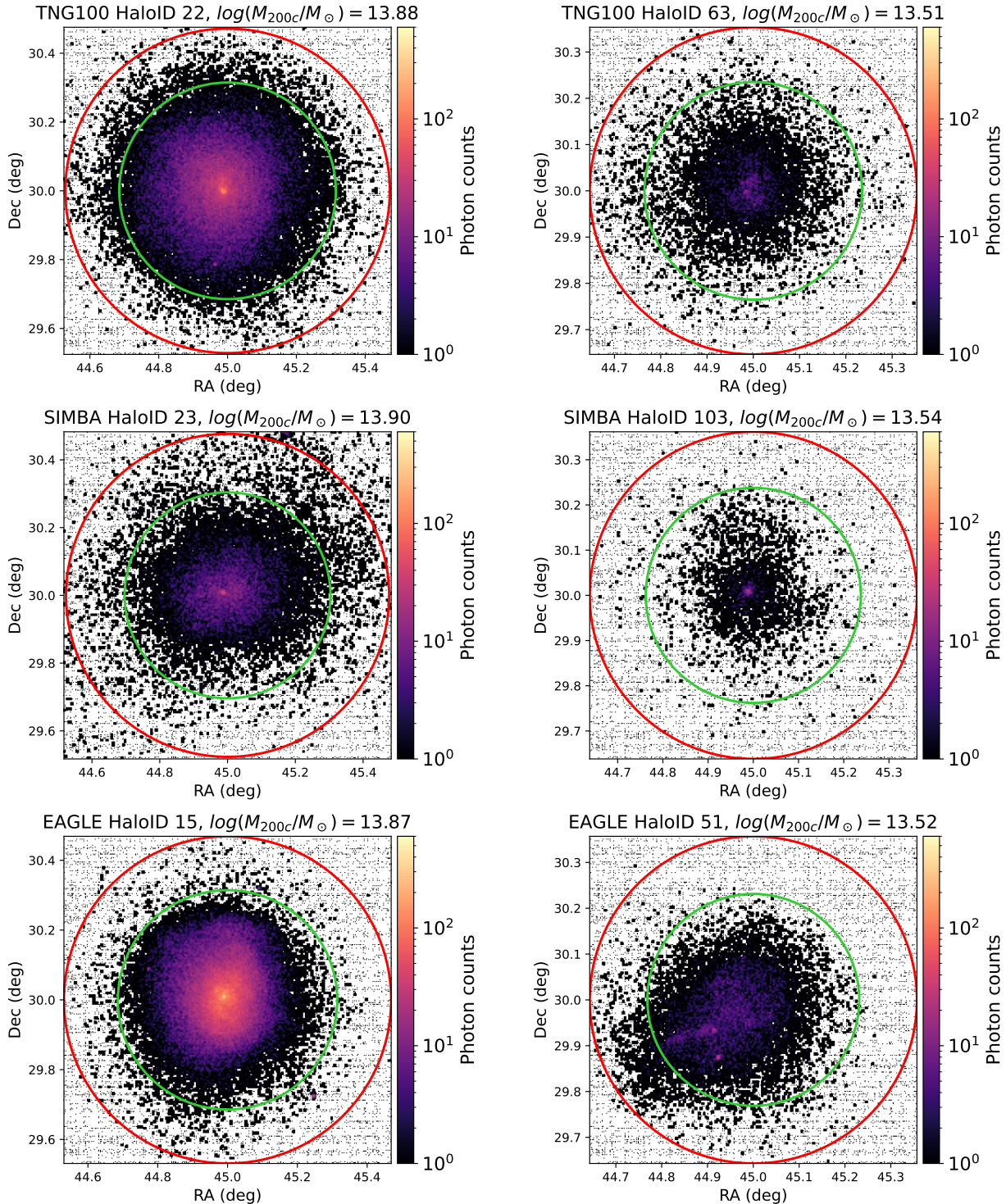


**Figure 4.1.** X-ray count maps of the Chandra mock observations. The red and green circles show the  $r_{200c}$  and  $r_{500c}$ , respectively, of each halo.

## 4.2 XMM-Newton mocks

### 4.2 XMM-Newton mocks

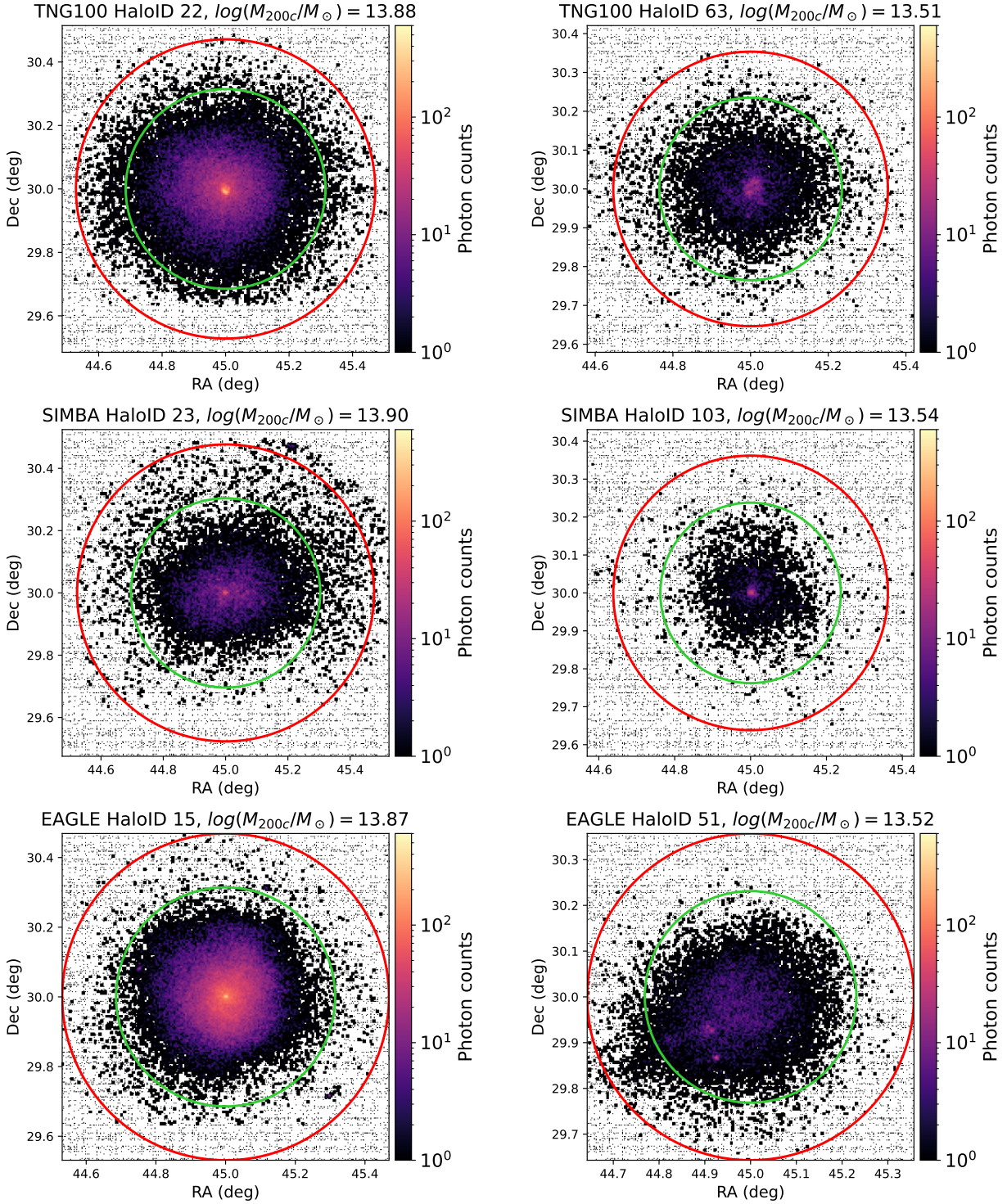


**Figure 4.2.** X-ray count maps of the XMM-Newton mock observations. The red and green circles show the  $r_{200c}$  and  $r_{500c}$ , respectively, of each halo.

### 4.3 eROSITA mocks

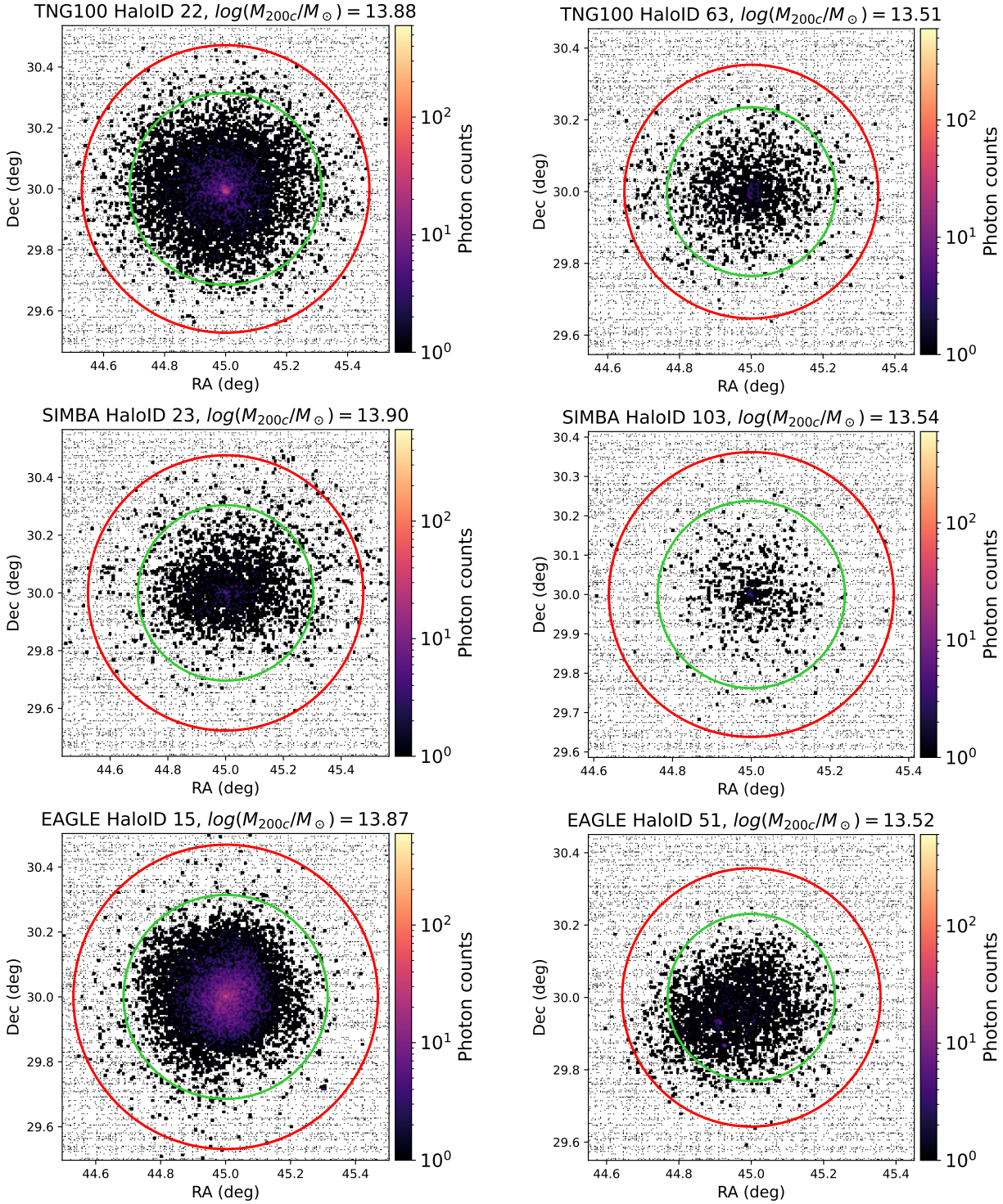


**Figure 4.3.** X-ray count maps of the eROSITA mock observations. The red and green circles show the  $r_{200c}$  and  $r_{500c}$ , respectively, of each halo

## 4.4 Mocked X-ray luminosity

Having compared the trends of the  $L_x - M$  relation in the simulations using the intrinsic  $L_x$  in Figure 2.12, we now look at the  $L_x - M$  relation in the three simulations with the mock-observed  $L_x$  in Figure 4.4, Figure 4.5, and Figure 4.6 for each telescope.

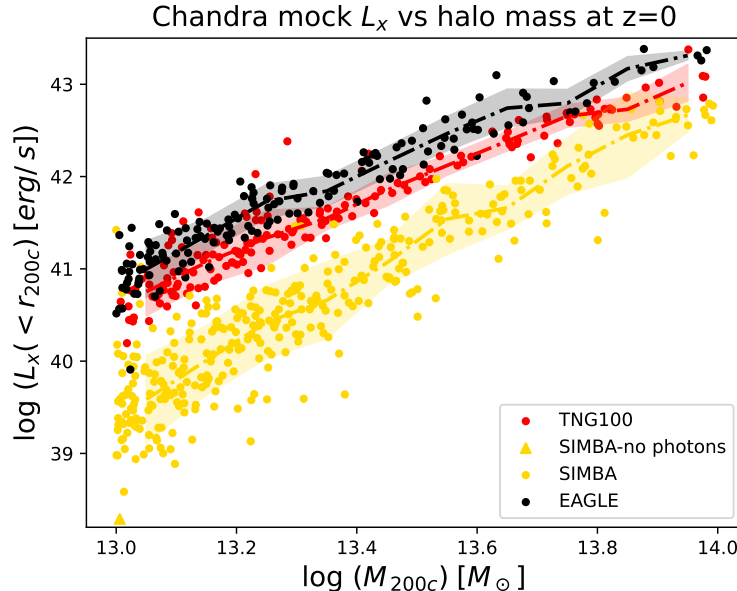


**Figure 4.4.** Comparing the Chandra mock-observed  $L_x - M$  relation of each simulation. Solid dots represent individual halos, dashed-dotted lines represent the running median values in bins of 0.1 dex, the shaded region is the  $1 - \sigma$  deviation, and the solid triangles plotted along the x-axis represent halos without any detected photons.

#### 4.4 Mocked X-ray luminosity

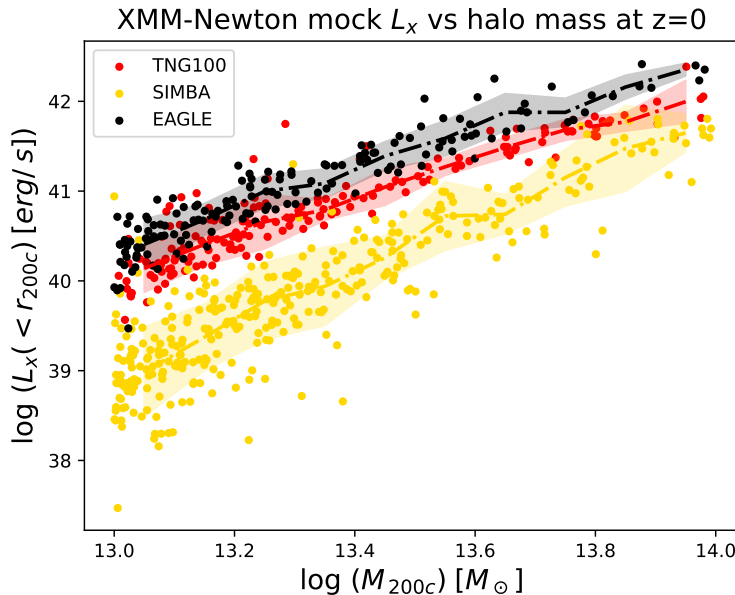


**Figure 4.5.** Comparing the XMM-Newton mock-observed  $L_x - M$  relation of each simulation. Solid dots represent individual halos, dashed-dotted lines represent the running median values in bins of 0.1 dex, and the shaded region is the  $1 - \sigma$  deviation.

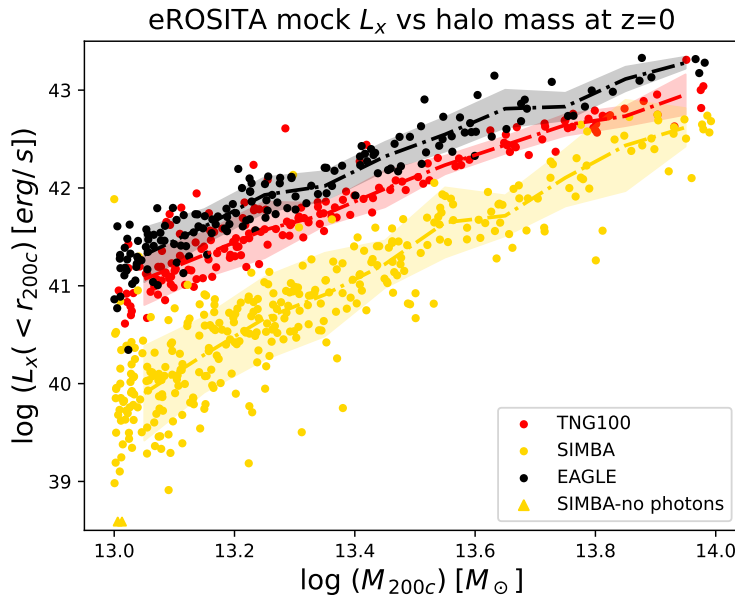


**Figure 4.6.** Comparing the eROSITA mock-observed  $L_x - M$  relation of each simulation. Solid dots represent individual halos, dashed-dotted lines represent the running median values in bins of 0.1 dex, the shaded region is the  $1 - \sigma$  deviation, and the solid triangles plotted along the x-axis represent halos without any detected photons.

The general trend is similar to that of the intrinsic  $L_x - M$  relation, with an overall offset in the total luminosity to lower values. To see how the intrinsic and the mock-

#### 4.4 Mocked X-ray luminosity

observed luminosities differ, we compare the two further. Due to potential differences in the plasma modeling of the 'APEC' model in the 'XSPEC' package used to calculate the intrinsic  $L_x$  and the 'pyXSIM' package used in the mocking procedure, this comparison isn't one-to-one exactly. But assuming only minor variations in the models, we compare the mocked  $L_x$  to the intrinsic  $L_x$  in Figure 4.7.

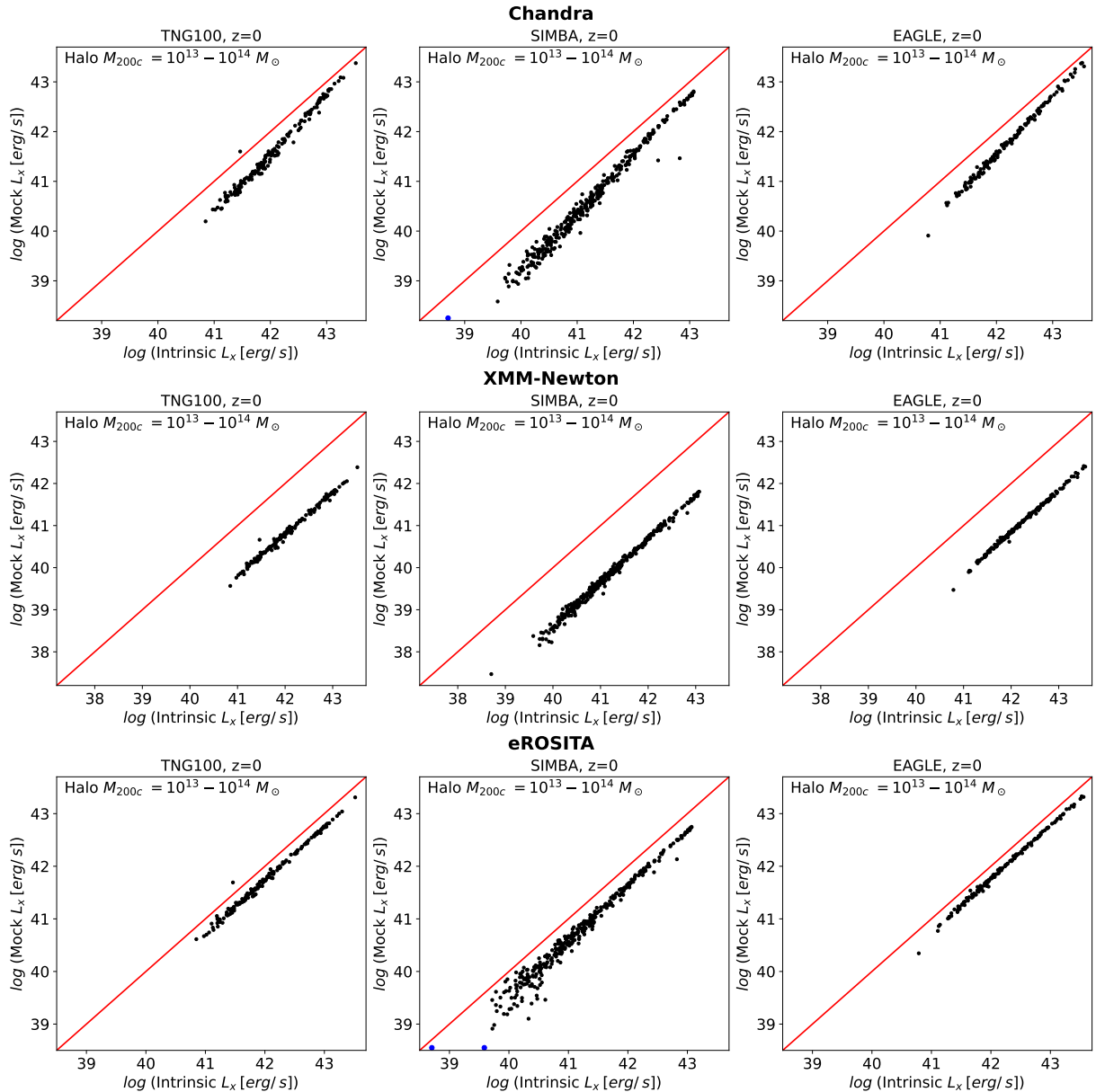


**Figure 4.7.** Mock vs intrinsic luminosity in each simulation. Halos, where the mock observation detected no photons in the soft band, are represented by blue dots plotted along the x-axis.

The mock-observed luminosity of halos is consistently lower than the intrinsic calculated luminosity (except for one outlier halo in TNG100, but this doesn't seem to be due

#### 4.4 Mocked X-ray luminosity

to underlying physics, as we are making a statistical analysis of our entire halo sample). This is expected as the observations lose data due to the instrumental limits. We look at the observed  $L_x$  as a percentage of the intrinsic  $L_x$  in Figure 4.8.

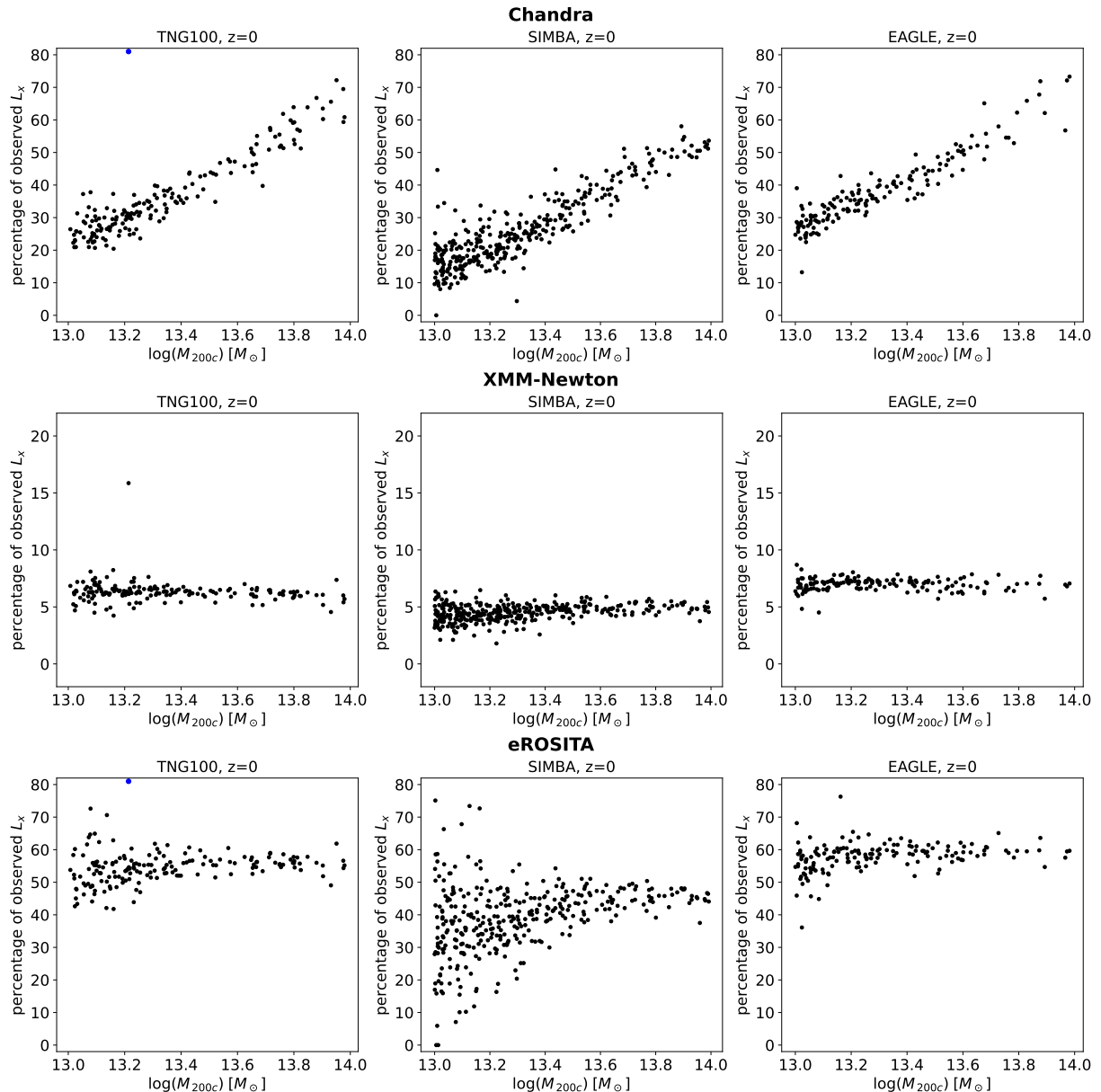


**Figure 4.8.** Percentage of observed luminosity as a function of halo mass in each simulation. Blue dots represent the outlier halo in TNG100 with 140% and 165% in Chandra and eROSITA respectively.

For the Chandra mocks, the percentage of the observed luminosity varies from 20% to 80% and increases with an increase in halo mass. Comparing the three simulations, TNG100 and EAGLE show a similar observed  $L_x$  percentage, while SIMBA has lower values, reaching up to 60% at the high mass end. For XMM-Newton mocks, the per-

centage is significantly lower than the other two telescopes, ranging only between 5% - 10%, and the values stay almost constant over the halo mass range. For eROSITA mocks, in TNG100 and EAGLE, the percentage is almost constant over the halo mass range, ranging between 40% and 75%, while the mocks for SIMBA halos show a large variation for the low mass halos, ranging from below 10% up to almost 80%.

## 4.5 Effects of detection on the inferred relationship between gas fraction and total mass

We would not detect a halo in a survey if its  $L_x$  is lower than the limiting  $L_x$  (obtained from the limiting flux) of the survey. Given the loss of  $L_x$  in the observed halos, we are more likely to miss the detection of a given halo in a survey using these telescopes compared to an analysis of the simulations. In this section, we look at the completeness fraction of our sample of halos in each simulation, and how detection affects the observational inference of the group gas fraction.

The surveys chosen for the analysis vary in completeness at varying flux limit values. To replicate this completeness fraction at the given flux limit, we first multiply the flux limit by  $4\pi d_L^2$  to calculate the  $L_x$  limit. Then, for all the halos that are above this limiting  $L_x$ , we apply a selection algorithm to randomly select a fraction of these halos such that it matches the completeness fraction.

### 4.5.1 Chandra

We choose the flux limit of  $3 \times 10^{-15}$  erg s $^{-1}$  cm $^{-2}$  (corresponding to a  $L_x$  limit of  $4.56 \times 10^{39}$  erg s $^{-1}$ ) from ([Vik+06]), which is a sample of 13 clusters observed by pointed observations with Chandra. For the flux limit, Figure 4.9 shows that all of the groups in TNG100 and EAGLE are detected, while the completeness fraction for SIMBA increases from 0.4 to 1.0 with increasing halo mass. Since we detect a majority of the groups, we do not see deviations from the trend seen in the intrinsic  $f_g - M$  relation (Figure 4.10), as expected.

#### 4.5 Effects of detection on the inferred relationship between gas fraction and total mass

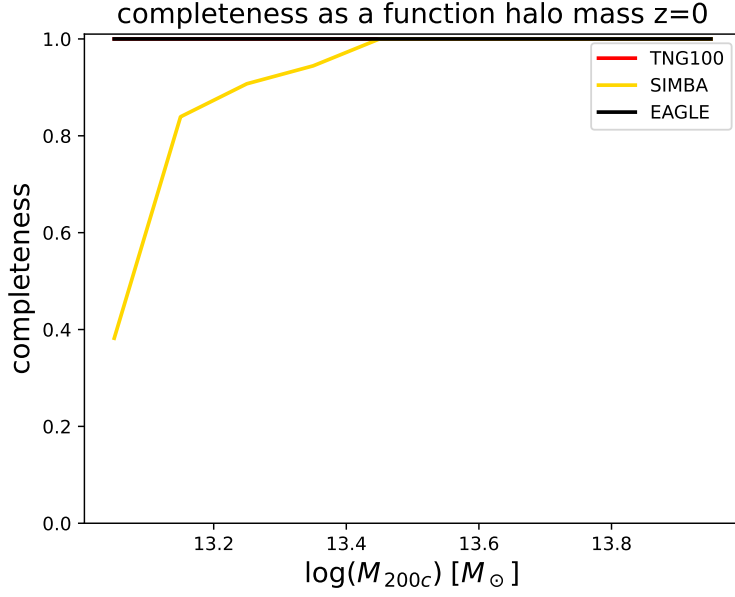


**Figure 4.9.** The fraction of groups detected, with the flux limit of  $3 * 10^{-15}$  erg s $^{-1}$  cm $^{-2}$ , over the total groups for each simulation as a function of the halo mass, calculated in bins of 0.1 dex.

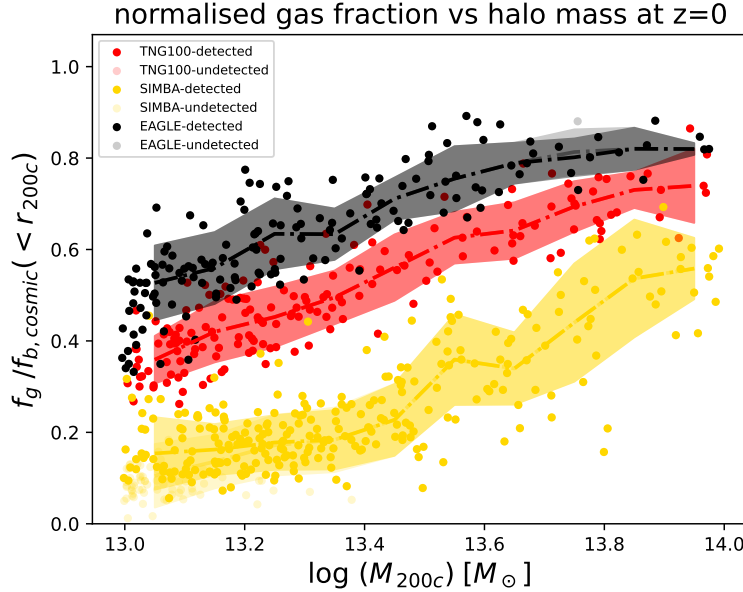


**Figure 4.10.** Comparing the  $f_g - M$  relation between the groups detected, with the flux limit of  $3 * 10^{-15}$  erg s $^{-1}$  cm $^{-2}$ , and all the groups in the simulations. The solid dots represent the detected groups and the faded dots represent the undetected groups. The dash-dotted lines (solid for detected groups and faded for total sample) represent the running median values in bins of 0.1 dex, and the shaded region shows the  $1 - \sigma$  deviation.

### 4.5.2 XMM-Newton

We choose the XXL survey cluster catalog ([Ada+18]) with a flux limit of  $1.3 * 10^{-14}$  erg s $^{-1}$  cm $^{-2}$  at 100 percent completeness, which corresponds to a  $L_x$  limit of  $1.97 * 10^{40}$  erg s $^{-1}$ . The completeness fraction increases with halo mass and reaches 1.0 quickly for TNG100 and EAGLE, and only at the high mass end for SIMBA (Figure 4.11). The  $f_g - M$  relation shows no variation between the detected and the total sample of groups for EAGLE and shows a small deviation in the median values for TNG100 at the low-mass end, but we still find an overlap within the  $1 - \sigma$  range. For SIMBA, there is a larger deviation in median values, while the  $1 - \sigma$  of the detected and total populations still overlap (Figure 4.12).

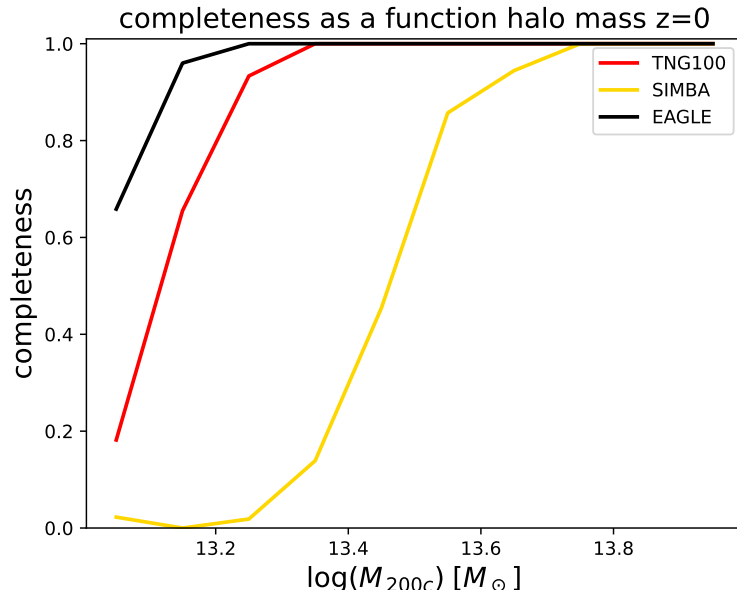


**Figure 4.11.** The fraction of groups detected, with the XMM-XXL flux limit of  $1.3 * 10^{-14}$  erg s $^{-1}$  cm $^{-2}$ , over the total groups for each simulation as a function of the halo mass, calculated in bins of 0.1 dex.

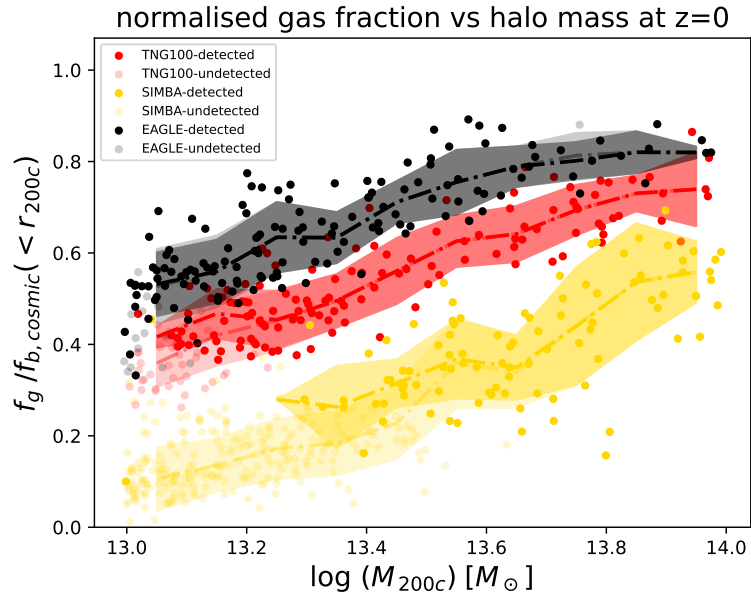


**Figure 4.12.** Comparing the  $f_g - M$  relation between the groups detected, with the XMM-XXL flux limit of  $1.3 * 10^{-14}$  erg s $^{-1}$  cm $^{-2}$ , and all the groups in the simulations. The solid dots represent the detected groups and the faded dots represent the undetected groups. The dash-dotted lines (solid for detected groups and faded for total sample) represent the running median values in bins of 0.1 dex, and the shaded region shows the  $1 - \sigma$  deviation.

### 4.5.3 eROSITA

We choose three different limits on the flux based on various surveys of groups and clusters with eROSITA. The first one is based on the eFEDS survey with a flux limit of  $10^{-14}$  erg s $^{-1}$  cm $^{-2}$  and completeness of 40 percent, corresponding to a  $L_x$  limit of  $1.52 * 10^{40}$  erg s $^{-1}$  ([Liu+22]). In Figure 4.13, we see the completeness fraction varying around 0.4 for each simulation. The  $f_g - M$  relation does not show significant deviation within the  $1 - \sigma$  range of the detected and total group populations (Figure 4.14).

#### 4.5 Effects of detection on the inferred relationship between gas fraction and total mass

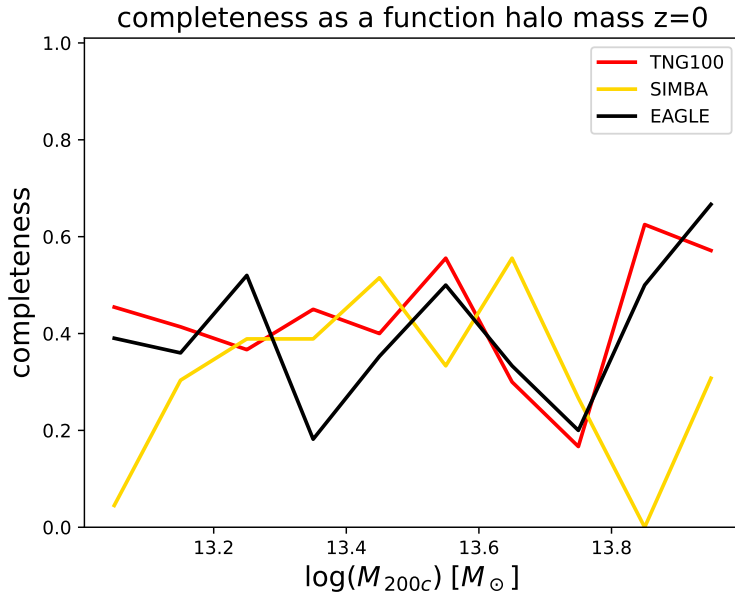


**Figure 4.13.** The fraction of groups detected, with the eFEDS flux limit of  $10^{-14} \text{ erg s}^{-1} \text{ cm}^{-2}$ , over the total groups for each simulation as a function of the halo mass, calculated in bins of 0.1 dex.

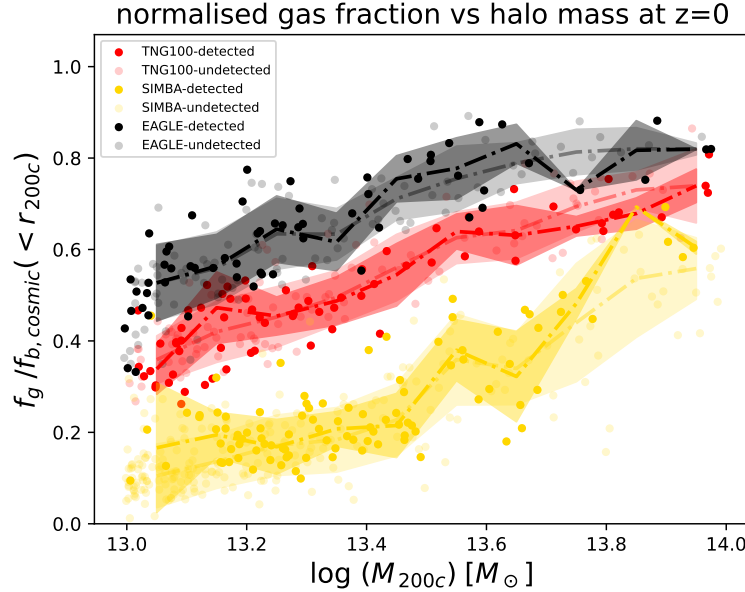


**Figure 4.14.** Comparing the  $f_g - M$  relation between the groups detected, with the eFEDS flux limit of  $10^{-14} \text{ erg s}^{-1} \text{ cm}^{-2}$ , and all the groups in the simulations. The solid dots represent the detected groups and the faded dots represent the undetected groups. The dash-dotted lines (solid for detected groups and faded for total sample) represent the running median values in bins of 0.1 dex, and the shaded region shows the  $1 - \sigma$  deviation.

#### 4.5 Effects of detection on the inferred relationship between gas fraction and total mass

The second flux limit is of  $8 * 10^{-13}$  erg s $^{-1}$  cm $^{-2}$  for a 90 percent complete sample from the eRASS1 survey ([Bul+24]), which corresponds to a  $L_x$  limit of  $1.21 * 10^{42}$  erg/s. For this limit, we mainly detect high mass groups (Figure 4.15), as the low mass groups are not bright enough to be detected (Figure 4.6) for the given  $L_x$  limit. The  $f_g - M$  relation is hence not comparable at the low-mass end of the population. Figure 4.16 shows overlap in the  $1 - \sigma$  in the detected and total group populations for all three simulations, while the median values show small deviations.

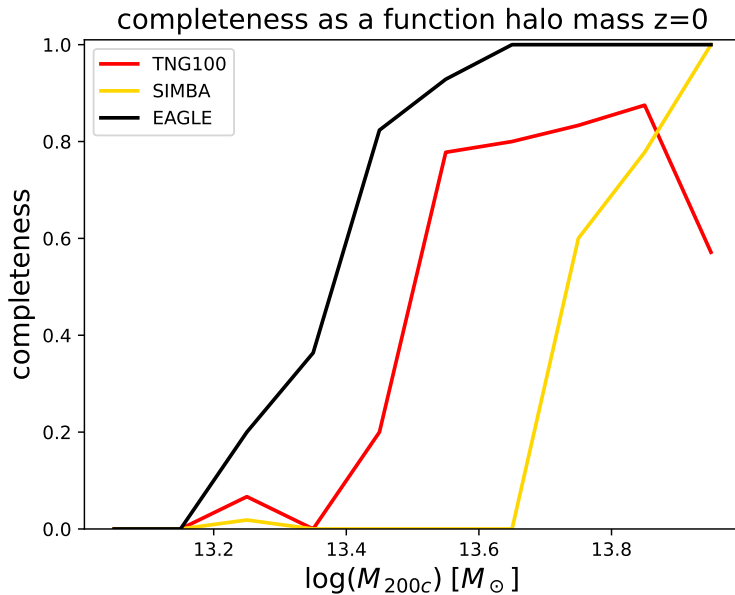


**Figure 4.15.** The fraction of groups detected, with the eRASS1 flux limit of  $8 * 10^{-13}$  erg s $^{-1}$  cm $^{-2}$ , over the total groups for each simulation as a function of the halo mass, calculated in bins of 0.1 dex.

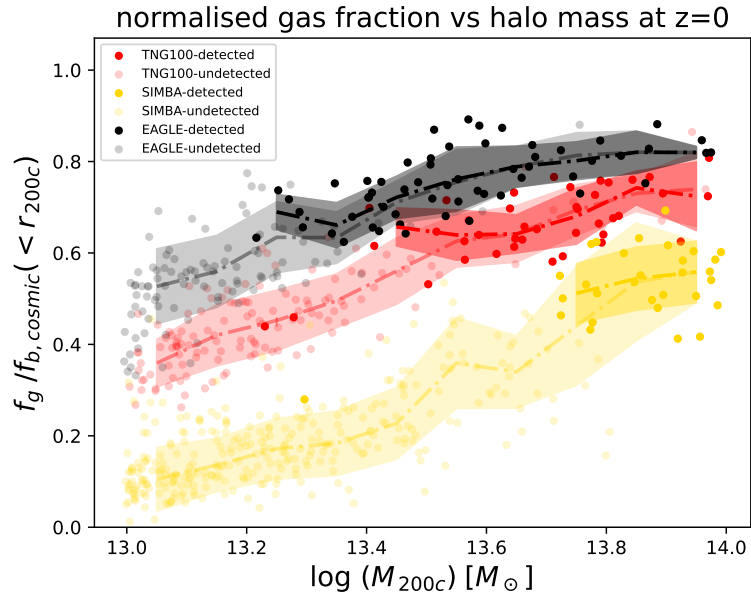


**Figure 4.16.** Comparing the  $f_g - M$  relation between the groups detected, with the eRASS1 flux limit of  $8 * 10^{-13}$  erg s $^{-1}$  cm $^{-2}$ , and all the groups in the simulations. The solid dots represent the detected groups and the faded dots represent the undetected groups. The dash-dotted lines (solid for detected groups and faded for total sample) represent the running median values in bins of 0.1 dex, and the shaded region shows the  $1 - \sigma$  deviation.

The third is a flux limit of  $10^{-13}$  erg s $^{-1}$  cm $^{-2}$  for a 30 percent complete sample from the eRASS1 cosmology catalog ([Bul+24]), corresponding to a  $L_x$  limit of  $1.52 * 10^{41}$  erg s $^{-1}$ . Again, we see a variation around a completeness fraction of 0.3, with lower completeness in the low-mass end and slightly higher completeness in the high-mass end (Figure 4.17). The detected and the total populations again show significant overlap in the  $1 - \sigma$  range, but the median values for SIMBA deviate at the low-mass end (Figure 4.18).

#### 4.5 Effects of detection on the inferred relationship between gas fraction and total mass

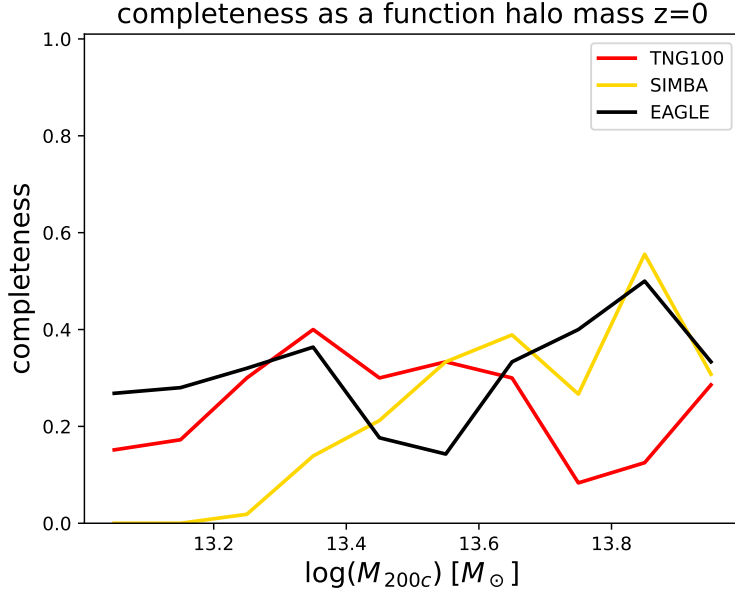


**Figure 4.17.** The fraction of groups detected, with the eRASS1-cosmology sample flux limit of  $10^{-13}$  erg s $^{-1}$  cm $^{-2}$ , over the total groups for each simulation as a function of the halo mass, calculated in bins of 0.1 dex.

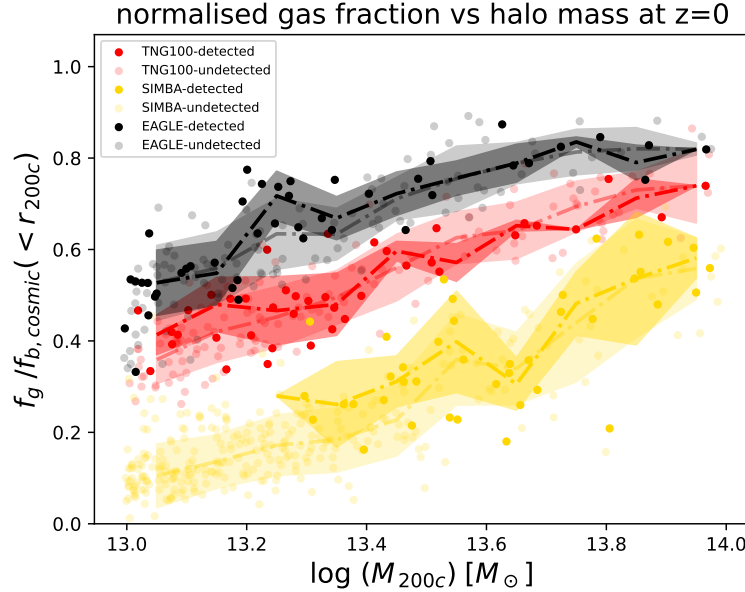


**Figure 4.18.** Comparing the  $f_g - M$  relation between the groups detected, with the eRASS1-cosmology sample flux limit of  $10^{-13}$  erg s $^{-1}$  cm $^{-2}$ , and all the groups in the simulations. The solid dots represent the detected groups and the faded dots represent the undetected groups. The dash-dotted lines (solid for detected groups and faded for total sample) represent the running median values in bins of 0.1 dex, and the shaded region shows the  $1 - \sigma$  deviation.

## 5 Summary, Conclusion, and Outlook

We analysed the gas content and its distribution in galaxy groups in three cosmological simulations: TNG100, EAGLE, and SIMBA. We discussed the different ways in which they model the physical processes that affect the gas distribution in groups, with the AGN feedback model being the dominant one. We then built part of a pipeline to create realistic mock observations of the simulated groups, which included mocking the observations for three different instruments: the ACIS I instrument of the Chandra observatory, the EPIC-pn instrument of XMM-Newton, and the eROSITA telescope.

With the mock observed galaxy groups, we calculated the total luminosity, and using various flux limits (and corresponding luminosity limits), we compared the total group populations to the populations of the detected groups from each simulation. With Chandra and XMM-Newton being targeted observations and having lower flux limits (or better sensitivity to low flux) lead to a large proportion of the groups of lower masses being detected, while eROSITA’s higher flux limits, due to its wide-field survey nature, show very low completeness for low-mass groups. Although due to the difference in the total number of detections for the telescopes being large ([Bul+24]; [Ada+18]; [Vik+06], [Sun+09]), studies with eROSITA show promising potential to probe the higher mass end of groups, leading to large statistics for better constraints, while it becomes even more important to understand the selection effects and account for them.

Next, we compared the  $f_g - M$  relation calculated from the intrinsic simulation data between the complete population and the detected one, finding the same overlap in the curves with deviations within the statistical bounds of  $1 - \sigma$  range of both populations. Except for a potential deviation in the detected sample from XMM-Newton and eROSITA for the group population in SIMBA, this implies that the observational effect of the detection of groups does not affect the  $f_g - M$  relation calculated from the simulation data. The consistency of the mean gas fraction profiles of samples has also been shown in the recent work of [Pop+24]. The X-ray selection effect was studied by also including optical detections, and comparing the X-ray detected vs undetected populations.

This analysis can be further built upon by continuing the mocking pipeline, so as to obtain the gas mass and the total mass within different apertures of the galaxy groups (for example,  $r_{500c}$ ,  $r_{2500c}$ , inner 300 kpc, etc.). This would mean adding background photons

### *Summary, Conclusion, and Outlook*

when creating the mocks, and then performing data reduction of the mock observed groups in line with the procedure of the observational survey. The background subtracted mocks can then be used to extract gas mass and total mass of the groups, as done in [Mar+24]. This would provide more realistic mocks of the simulated groups, and then the data can be analysed and compared to that obtained by X-ray observational surveys to study the various effects and biases affecting the results and conclusions drawn. Other gas properties of the IGrM, such as the  $kT - L_x$  relation can also be studied with the mock-observed groups, thus helping us put tighter constraints on the physics governing the gas content and its distribution in groups and clusters, followed by an improved understanding of the large scale structure, and hence cosmology.

## **6 Acknowledgements**

First and foremost, I am deeply grateful to Urmila Chadayammuri and Annalisa Pillepich for their guidance throughout the thesis. Their patience and insightful mentorship were instrumental in the successful completion of my project. I extend my sincere thanks to the Max Planck Institute for Astronomy (MPIA) for fostering an accommodating and stimulating research environment.

I would also like to thank my colleagues in the group and across the university for their discussions that made my study and research experience truly enjoyable. I am grateful to Ashish, Caro, Janhavi, Joey, Lutz, and Maitri who proofread parts of my thesis and provided me with valuable suggestions. I am also grateful to Maitri for being a constant support in many ways.

I would also like to thank my friends Ashish, Atharv, and Prasad together with whom my motivation and understanding of physics prospered. And finally, I am grateful to my family for the sacrifices that they have made over the years to enable me to pursue my Master's degree at Heidelberg University.

# Bibliography

- [Ada+18] C. Adami et al. “The XXL Survey. XX. The 365 cluster catalogue”. In: 620, A5 (Nov. 2018), A5. doi: [10.1051/0004-6361/201731606](https://doi.org/10.1051/0004-6361/201731606). arXiv: [1810.03849](https://arxiv.org/abs/1810.03849) [[astro-ph.CO](#)].
- [Ang+17] Daniel Anglés-Alcázar et al. “Gravitational torque-driven black hole growth and feedback in cosmological simulations”. In: 464.3 (Jan. 2017), pp. 2840–2853. doi: [10.1093/mnras/stw2565](https://doi.org/10.1093/mnras/stw2565). arXiv: [1603.08007](https://arxiv.org/abs/1603.08007) [[astro-ph.GA](#)].
- [ANP23] Mohammadreza Ayromlou, Dylan Nelson, and Annalisa Pillepich. “Feedback reshapes the baryon distribution within haloes, in halo outskirts, and beyond: the closure radius from dwarfs to massive clusters”. In: 524.4 (Oct. 2023), pp. 5391–5410. doi: [10.1093/mnras/stad2046](https://doi.org/10.1093/mnras/stad2046). arXiv: [2211.07659](https://arxiv.org/abs/2211.07659) [[astro-ph.GA](#)].
- [BDC12] H. Böhringer, K. Dolag, and G. Chon. “Modelling self-similar appearance of galaxy clusters in X-rays”. In: 539, A120 (2012), A120. doi: [10.1051/0004-6361/201118000](https://doi.org/10.1051/0004-6361/201118000). arXiv: [1112.5035](https://arxiv.org/abs/1112.5035) [[astro-ph.CO](#)].
- [BH44] H. Bondi and F. Hoyle. “On the mechanism of accretion by stars”. In: 104 (Jan. 1944), p. 273. doi: [10.1093/mnras/104.5.273](https://doi.org/10.1093/mnras/104.5.273).
- [BH86] Josh Barnes and Piet Hut. “A hierarchical O( $N \log N$ ) force-calculation algorithm”. In: 324.6096 (Dec. 1986), pp. 446–449. doi: [10.1038/324446a0](https://doi.org/10.1038/324446a0).
- [Bon52] H. Bondi. “On spherically symmetrical accretion”. In: 112 (Jan. 1952), p. 195. doi: [10.1093/mnras/112.2.195](https://doi.org/10.1093/mnras/112.2.195).
- [Bru+22] H. Brunner et al. “The eROSITA Final Equatorial Depth Survey (eFEDS). X-ray catalogue”. In: 661, A1 (2022), A1. doi: [10.1051/0004-6361/202141266](https://doi.org/10.1051/0004-6361/202141266). arXiv: [2106.14517](https://arxiv.org/abs/2106.14517) [[astro-ph.HE](#)].
- [Bul+24] E. Bulbul et al. “The SRG/eROSITA All-Sky Survey. The first catalog of galaxy clusters and groups in the Western Galactic Hemisphere”. In: 685, A106 (May 2024), A106. doi: [10.1051/0004-6361/202348264](https://doi.org/10.1051/0004-6361/202348264). arXiv: [2402.08452](https://arxiv.org/abs/2402.08452) [[astro-ph.CO](#)].

## Bibliography

- [Cra+15] Robert A. Crain et al. “The EAGLE simulations of galaxy formation: calibration of subgrid physics and model variations”. In: 450.2 (June 2015), pp. 1937–1961. DOI: 10.1093/mnras/stv725. arXiv: 1501.01311 [astro-ph.GA].
- [Dau+19] Thomas Dauser et al. “SIXTE: a generic X-ray instrument simulation toolkit”. In: 630, A66 (Sept. 2019), A66. DOI: 10.1051/0004-6361/201935978. arXiv: 1908.00781 [astro-ph.HE].
- [Dav+19] Romeel Davé et al. “SIMBA: Cosmological simulations with black hole growth and feedback”. In: 486.2 (2019), pp. 2827–2849. DOI: 10.1093/mnras/stz937. arXiv: 1901.10203 [astro-ph.GA].
- [DTH16] Romeel Davé, Robert Thompson, and Philip F. Hopkins. “MUFASA: galaxy formation simulations with meshless hydrodynamics”. In: 462.3 (Nov. 2016), pp. 3265–3284. DOI: 10.1093/mnras/stw1862. arXiv: 1604.01418 [astro-ph.GA].
- [ELS20] S. Ettori, L. Lovisari, and M. Sereno. “From universal profiles to universal scaling laws in X-ray galaxy clusters”. In: 644, A111 (2020), A111. DOI: 10.1051/0004-6361/202038586. arXiv: 2010.04192 [astro-ph.CO].
- [Gar+03] Gordon P. Garmire et al. “Advanced CCD imaging spectrometer (ACIS) instrument on the Chandra X-ray Observatory”. In: *X-Ray and Gamma-Ray Telescopes and Instruments for Astronomy*. Ed. by Joachim E. Truemper and Harvey D. Tananbaum. Vol. 4851. Society of Photo-Optical Instrumentation Engineers (SPIE) Conference Series. Mar. 2003, pp. 28–44. DOI: 10.1117/12.461599.
- [HE81] R. W. Hockney and J. W. Eastwood. *Computer Simulation Using Particles*. New York: McGraw-Hill, 1981.
- [Hop15] Philip F. Hopkins. “A new class of accurate, mesh-free hydrodynamic simulation methods”. In: 450.1 (June 2015), pp. 53–110. DOI: 10.1093/mnras/stv195. arXiv: 1409.7395 [astro-ph.CO].
- [HQ11] Philip F. Hopkins and Eliot Quataert. “An analytic model of angular momentum transport by gravitational torques: from galaxies to massive black holes”. In: 415.2 (Aug. 2011), pp. 1027–1050. DOI: 10.1111/j.1365-2966.2011.18542.x. arXiv: 1007.2647 [astro-ph.CO].
- [Jan+01] F. Jansen et al. “XMM-Newton observatory. I. The spacecraft and operations”. In: 365 (2001), pp. L1–L6. DOI: 10.1051/0004-6361:20000036. URL: <https://ui.adsabs.harvard.edu/abs/2001A&A...365L...1J>.
- [Kai86] N. Kaiser. “Evolution and clustering of rich clusters.” In: 222 (1986), pp. 323–345. DOI: 10.1093/mnras/222.2.323.

## Bibliography

- [Liu+22] A. Liu et al. “The eROSITA Final Equatorial-Depth Survey (eFEDS). Catalog of galaxy clusters and groups”. In: 661, A2 (2022), A2. DOI: 10.1051/0004-6361/202141120. arXiv: 2106.14518 [astro-ph.CO].
- [LJS12] David H. Lumb, Fred A. Jansen, and Norbert Schartel. “X-ray Multi-mirror Mission (XMM-Newton) observatory”. In: *Optical Engineering* 51.1 (2012), p. 011009. DOI: 10.1117/1.OE.51.1.011009. URL: <https://doi.org/10.1117/1.OE.51.1.011009>.
- [Lov+21] Lorenzo Lovisari et al. “Scaling Properties of Galaxy Groups”. In: *Universe* 7.5, 139 (2021), p. 139. DOI: 10.3390/universe7050139. arXiv: 2106.13256 [astro-ph.CO].
- [Mar+24] I. Marini et al. “Detecting galaxy groups populating the local Universe in the eROSITA era”. In: 689, A7 (Sept. 2024), A7. DOI: 10.1051/0004-6361/202450442. arXiv: 2404.12719 [astro-ph.CO].
- [Mer+24] A. Merloni et al. “The SRG/eROSITA all-sky survey. First X-ray catalogues and data release of the western Galactic hemisphere”. In: 682, A34 (Feb. 2024), A34. DOI: 10.1051/0004-6361/202347165. arXiv: 2401.17274 [astro-ph.HE].
- [Nel+19] Dylan Nelson et al. “First results from the TNG50 simulation: galactic outflows driven by supernovae and black hole feedback”. In: 490.3 (Dec. 2019), pp. 3234–3261. DOI: 10.1093/mnras/stz2306. arXiv: 1902.05554 [astro-ph.GA].
- [PBS11] Ruediger Pakmor, Andreas Bauer, and Volker Springel. “Magnetohydrodynamics on an unstructured moving grid”. In: 418.2 (Dec. 2011), pp. 1392–1401. DOI: 10.1111/j.1365-2966.2011.19591.x. arXiv: 1108.1792 [astro-ph.IM].
- [Pil+18] Annalisa Pillepich et al. “Simulating galaxy formation with the IllustrisTNG model”. In: 473.3 (2018), pp. 4077–4106. DOI: 10.1093/mnras/stx2656. arXiv: 1703.02970 [astro-ph.GA].
- [Pil+21] Annalisa Pillepich et al. “X-ray bubbles in the circumgalactic medium of TNG50 Milky Way- and M31-like galaxies: signposts of supermassive black hole activity”. In: 508.4 (Dec. 2021), pp. 4667–4695. DOI: 10.1093/mnras/stab2779. arXiv: 2105.08062 [astro-ph.GA].
- [Pla+20] Planck Collaboration et al. “Planck 2018 results. VI. Cosmological parameters”. In: 641, A6 (Sept. 2020), A6. DOI: 10.1051/0004-6361/201833910. arXiv: 1807.06209 [astro-ph.CO].

## Bibliography

- [Pop+24] P. Popesso et al. “The X-ray invisible Universe. A look into the haloes undetected by eROSITA”. In: 527.1 (Jan. 2024), pp. 895–910. DOI: [10.1093/mnras/stad3253](https://doi.org/10.1093/mnras/stad3253). arXiv: [2302.08405](https://arxiv.org/abs/2302.08405) [astro-ph.CO].
- [Pre+21] P. Predehl et al. “The eROSITA X-ray telescope on SRG”. In: 647, A1 (2021), A1. DOI: [10.1051/0004-6361/202039313](https://doi.org/10.1051/0004-6361/202039313). arXiv: [2010.03477](https://arxiv.org/abs/2010.03477) [astro-ph.HE].
- [Ros+15] Y. M. Rosas-Guevara et al. “The impact of angular momentum on black hole accretion rates in simulations of galaxy formation”. In: 454.1 (Nov. 2015), pp. 1038–1057. DOI: [10.1093/mnras/stv2056](https://doi.org/10.1093/mnras/stv2056). arXiv: [1312.0598](https://arxiv.org/abs/1312.0598) [astro-ph.CO].
- [Sch+15a] Matthieu Schaller et al. “The EAGLE simulations of galaxy formation: the importance of the hydrodynamics scheme”. In: 454.3 (Dec. 2015), pp. 2277–2291. DOI: [10.1093/mnras/stv2169](https://doi.org/10.1093/mnras/stv2169). arXiv: [1509.05056](https://arxiv.org/abs/1509.05056) [astro-ph.GA].
- [Sch+15b] Joop Schaye et al. “The EAGLE project: simulating the evolution and assembly of galaxies and their environments”. In: 446.1 (2015), pp. 521–554. DOI: [10.1093/mnras/stu2058](https://doi.org/10.1093/mnras/stu2058). arXiv: [1407.7040](https://arxiv.org/abs/1407.7040) [astro-ph.GA].
- [Smi+01] Randall K. Smith et al. “Collisional Plasma Models with APEC/APED: Emission-Line Diagnostics of Hydrogen-like and Helium-like Ions”. In: 556.2 (Aug. 2001), pp. L91–L95. DOI: [10.1086/322992](https://doi.org/10.1086/322992). arXiv: [astro-ph/0106478](https://arxiv.org/abs/astro-ph/0106478) [astro-ph].
- [Sor+22] Daniele Sorini et al. “How baryons affect haloes and large-scale structure: a unified picture from the SIMBA simulation”. In: 516.1 (Oct. 2022), pp. 883–906. DOI: [10.1093/mnras/stac2214](https://doi.org/10.1093/mnras/stac2214). arXiv: [2111.13708](https://arxiv.org/abs/2111.13708) [astro-ph.GA].
- [Spr05] Volker Springel. “The cosmological simulation code GADGET-2”. In: 364.4 (Dec. 2005), pp. 1105–1134. DOI: [10.1111/j.1365-2966.2005.09655.x](https://doi.org/10.1111/j.1365-2966.2005.09655.x). arXiv: [astro-ph/0505010](https://arxiv.org/abs/astro-ph/0505010) [astro-ph].
- [Spr10] Volker Springel. “E pur si muove: Galilean-invariant cosmological hydrodynamical simulations on a moving mesh”. In: 401.2 (Jan. 2010), pp. 791–851. DOI: [10.1111/j.1365-2966.2009.15715.x](https://doi.org/10.1111/j.1365-2966.2009.15715.x). arXiv: [0901.4107](https://arxiv.org/abs/0901.4107) [astro-ph.CO].
- [Str+01] L. Strüder et al. “The European Photon Imaging Camera on XMM-Newton: The pn-CCD camera”. In: 365 (2001), pp. L18–L26. DOI: [10.1051/0004-6361:20000066](https://doi.org/10.1051/0004-6361:20000066).

## Bibliography

- [Sun+09] M. Sun et al. “Chandra Studies of the X-Ray Gas Properties of Galaxy Groups”. In: 693.2 (Mar. 2009), pp. 1142–1172. DOI: [10.1088/0004-637X/693/2/1142](https://doi.org/10.1088/0004-637X/693/2/1142). arXiv: [0805.2320](https://arxiv.org/abs/0805.2320) [astro-ph].
- [Tur+01] M. J. L. Turner et al. “The European Photon Imaging Camera on XMM-Newton: The MOS cameras”. In: 365 (Jan. 2001), pp. L27–L35. DOI: [10.1051/0004-6361:20000087](https://doi.org/10.1051/0004-6361:20000087). arXiv: [astro-ph/0011498](https://arxiv.org/abs/astro-ph/0011498) [astro-ph].
- [Vik+06] A. Vikhlinin et al. “Chandra Sample of Nearby Relaxed Galaxy Clusters: Mass, Gas Fraction, and Mass-Temperature Relation”. In: 640.2 (Apr. 2006), pp. 691–709. DOI: [10.1086/500288](https://doi.org/10.1086/500288). arXiv: [astro-ph/0507092](https://arxiv.org/abs/astro-ph/0507092) [astro-ph].
- [Vog+14] Mark Vogelsberger et al. “Introducing the Illustris Project: simulating the coevolution of dark and visible matter in the Universe”. In: 444.2 (Oct. 2014), pp. 1518–1547. DOI: [10.1093/mnras/stu1536](https://doi.org/10.1093/mnras/stu1536). arXiv: [1405.2921](https://arxiv.org/abs/1405.2921) [astro-ph.CO].
- [Vog+20] Mark Vogelsberger et al. “Cosmological simulations of galaxy formation”. In: *Nature Reviews Physics* 2.1 (Jan. 2020), pp. 42–66. DOI: [10.1038/s42254-019-0127-2](https://doi.org/10.1038/s42254-019-0127-2). arXiv: [1909.07976](https://arxiv.org/abs/1909.07976) [astro-ph.GA].
- [Wei+02] M. C. Weisskopf et al. “An Overview of the Performance and Scientific Results from the Chandra X-Ray Observatory”. In: 114.791 (2002), pp. 1–24. DOI: [10.1086/338108](https://doi.org/10.1086/338108). arXiv: [astro-ph/0110308](https://arxiv.org/abs/astro-ph/0110308) [astro-ph].
- [Wei+17] Rainer Weinberger et al. “Simulating galaxy formation with black hole driven thermal and kinetic feedback”. In: 465.3 (Mar. 2017), pp. 3291–3308. DOI: [10.1093/mnras/stw2944](https://doi.org/10.1093/mnras/stw2944). arXiv: [1607.03486](https://arxiv.org/abs/1607.03486) [astro-ph.GA].
- [Wri+24] Ruby J. Wright et al. “The baryon cycle in modern cosmological hydrodynamical simulations”. In: 532.3 (Aug. 2024), pp. 3417–3440. DOI: [10.1093/mnras/stae1688](https://doi.org/10.1093/mnras/stae1688). arXiv: [2402.08408](https://arxiv.org/abs/2402.08408) [astro-ph.GA].

## **Declaration of Authorship**

I hereby declare that I have written this thesis independently and have not used any sources or aids other than those stated. AI-based tools such as ChatGPT and Gemini were used to help with editing code and for language translations.

A handwritten signature in black ink, appearing to read "Maulik Deepen Parekh".

---

Maulik Deepen Parekh  
Heidelberg, January 10, 2025